Article:
Banks, DA orcid.org/0000-0001-9118-5298, Bozkaya, G and Bozkaya, O (2019) Direct Observation and Measurement of Au and Ag in Epithermal Mineralizing Fluids. Ore Geology Reviews, 111. 102955. ISSN 0169-1368

https://doi.org/10.1016/j.oregeorev.2019.102955

Accepted Manuscript

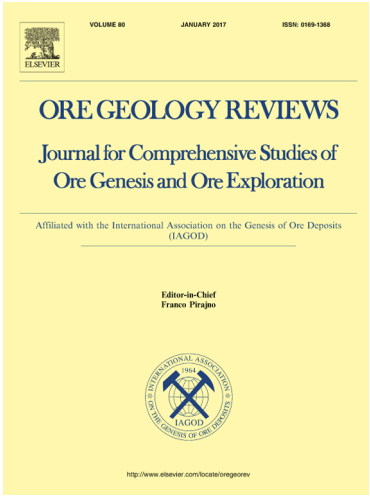

Direct Observation and Measurement of Au and Ag in Epithermal Mineralizing Fluids

David A. Banks, Gulcan Bozkaya, Omer Bozkaya

PII: S0169-1368(18)30754-6
DOI: https://doi.org/10.1016/j.oregeorev.2019.102955
Article Number: 102955
Reference: OREGEO 102955

To appear in: *Ore Geology Reviews*

Received Date: 30 August 2018
Revised Date: 15 May 2019
Accepted Date: 3 June 2019

Please cite this article as: D.A. Banks, G. Bozkaya, O. Bozkaya, Direct Observation and Measurement of Au and Ag in Epithermal Mineralizing Fluids, *Ore Geology Reviews* (2019), doi: https://doi.org/10.1016/j.oregeorev.2019.102955

Direct Observation and Measurement of Au and Ag in Epithermal Mineralizing Fluids

David A. Banks[1], Gulcan Bozkaya[2] & Omer Bozkaya[2]

[1]School of Earth and Environment, University of Leeds, Leeds, LS2 9JT, UK.
d.a.banks@leeds.ac.uk

[2] Pamukkale University, Department of Geological Engineering, 20070 Denizli, Turkey.

Abstract

Colloidal gold particles have been observed in c. 300 ^{O}C low salinity fluids from the Arapucandere intermediate sulphidation epithermal base-metal-Au deposit in NW Turkey. This is the first time colloidal gold has been recorded in an ancient mineralizing fluid. Growth, in veins, of large euhedral quartz crystals, after the deposition of sulphides, occurred in a number of stages from the introduction of fresh pulses of fluid. The quartz overgrowths have a fibrous texture which facilitated trapping of large elongate fluid inclusions between the quartz fibres which grew perpendicular to the crystal faces of the pre-existing quartz. Episodic periods of intense trapping of fluid inclusions occurred throughout the growth of quartz. Trapped within primary fluid inclusions are numerous particles of gold, the largest observed is c. 1 μm but most are smaller. BSE element mapping shows these to contain Au, Ag, Cu ± Hg. LA-ICP-MS profiles of the fluid inclusions confirm Au and Ag is not present in solution, being present as numerous particles. We have quantified the concentration of gold in fluid inclusions which are orders of magnitude greater than has been previously measured or thought likely in crustal fluids. The average Ag concentration is c. 32 ppm and Au is c. 41 ppm but the maximum concentrations of both may reach several 100's to 1000 ppm. Calcite forms a coating on the inner surface of the inclusions and barite, pyrite, galena, sphalerite and unidentified minerals are also present with the Au-Ag particles. It is clear that the Au-Ag particles could not have precipitated in the fluid inclusions, therefore they must have precipitated elsewhere and been carried with the hydrothermal fluid. The high concentrations and their colloidal nature have implications for the enrichment of gold in mineral deposits.

Keywords. Fluid inclusions, Colloidal gold, LA-ICP-MS, Epithermal, Turkey

1. Introduction

The generation of world class ore deposits relies on many factors (Simmons and Brown, 2006; Richards, 2013), but key aspects are the concentration of the metal in the ore fluid, the duration of the mineralizing system and how efficient the depositional process was. Mineralization involving most metals depends on transportation by chloride complexes and interaction with a source of reduced sulphur to precipitate metallic sulphides (Reed and Palandri, 2006). However, although Au can be transported as chloride complexes (Pokrovski et al. 2014; Williams-Jones et al. 2009), transportation as bi-sulphide complexes (Benning and Seward, 1996: Gammons and Williams-Jones, 1997; Zezin et al. 2011) is more efficient. Its deposition as a native metal or an alloy, primarily with Ag, requires a different set of processes. Breakdown of the $AuHS^-$ complex can be achieved by sulphidation of wallrocks to produce transition metal sulphides, but perhaps more commonly by changes in the P-T conditions of the mineralizing fluid. Small changes in fluid pressure lead to the production of an H_2S gas phase and deposition of native Au-Ag particles. Indeed boiling zones in ore deposits are commonly sites of high grade mineralization (Canet et al. 2011). Gold particles have been found in precipitates from volcanic gases (Taran et al. 2000; Yudovskaya et al. 2006) and Gartman et al. (2018) have recorded sub-micron colloidal gold particles in the cooled fluids from actively boiling black smokers.

One of the major classifications of gold mineralization is that of epithermal systems which are spatially related to porphyritic igneous intrusions at depth. A link between porphyry-epithermal deposits and arc volcanism (Tosdal et al. 2009; Nadeau et al. 2016), can be established from the similarity in the compositions of the magmatic vapours and fluid inclusion compositions from the ore deposits. There is also transition from lithostatic pressure, during the non-eruptive phase of volcanism and porphyry systems, to a rapid pressure decrease, which results in a volcanic eruptive phase and in cooling of magmatic vapour through adiabatic expansion which leads to metal deposition in the ore deposits. In epithermal mineralized systems low density magmatic vapour or low salinity liquids ascend to within c. 1 km of the surface (Heinrich et al. 200; Heinrich et al. 2005; Pudack et al. 2009; Berger and Henley, 2011; Henley and Berger, 2011; Hurtig and Williams-Jones, 2015) where by a number of processes, gold and other precious metals may precipitate in vein systems. However, the concentrations of gold are usually very low and difficult to determine in fluid inclusions. The inability to measure gold concentrations in fluid inclusions was a fundamental problem in understanding key processes that transport and precipitate the metal. Recent technology advances now allow direct measurement of Au concentrations in the ore-

forming fluids trapped in various minerals as fluid inclusions. Data from porphyry and epithermal systems show that Au may be present at the ppm level (Ulrich et. al. 1999) in fluid inclusions over a range of temperatures, but this is in contrast to contemporaneous fluids from high temperature geothermal systems or volcanic gases, where concentrations can be orders of magnitude less, in the ppb range (Taran et al. 2000; Hannington et al. 2016). Such fluids are geologically equivalent but clearly there is a concentration issue either related to the source of fluids and gold or to a different set of processes that operate in ore deposits. The $AuHS^{-}$ complex is pressure sensitive and a small pressure change can induce almost complete removal of Au from solution (Sanchez-Alfaro et al. 2016). It has been suggested that Au colloids can transport gold and textures of the "bonanza" veinlets are consistent with the transport of gold colloids forming larger aggregates (Saunders, 1990; Herrington and Wilkinson, 1993). There has been no direct evidence for the production and transport of colloidal-size Au particles in hydrothermal fluids until Gartman et al. (2018) discovered colloidal gold resulting from black smoker fluids that had boiled and exhaled into the cold seawater.

This study provides evidence for the presence of colloidal Au-Ag particles in epithermal fluids. These were observed using scanning electron microscopy (SEM), in primary fluid inclusions that were trapped during the growth of large quartz crystals. SEM cathodoluminescence (SEM-CL) was used to define the multiple growth stages of the quartz which were linked to different generations of largely primary fluid inclusions, which record rapid changes in pressure and temperature. Microthermometry of the fluid inclusions constrained pressure, temperature and salinity of the hydrothermal fluids over the period of euhedral quartz growth. Combining the salinity of the fluid inclusions with laser ablation-inductively coupled plasma-mass spectrometry (LA-ICP-MS) analyses of individual fluid inclusions allowed the concentration of Au and Ag to be determined. In addition the LA-ICP-MS profiles showed in what form Au and Ag were present in the fluid inclusions.

2. Geological Setting

Western Turkey is part of the Tethyan Metallogenic Belt (Jankovic, 1986; Jingwen et. al. 2013; Richards, 2015) and contains porphyry and epithermal mineralized areas linked to subduction-related magmatism from the closure of the Tethys Ocean (Yigit, 2006; 2009). In the Biga Peninsula (Okay et al. 1990; Yilmaz et al. 1990; Ercan et al. 1995; Sanchez et al.

2013; Bertrand et al. 2014) this has resulted in numerous, predominantly, epithermal deposits, of low, intermediate and high sulphidation styles and porphyry deposits, making this region, perhaps, the most important for exploitation and exploration in the near east/Europe (Yigit, 2012). The deposits are relatively closely spaced, of variable size and may have gold as the sole resource, while others are base-metal resources with lesser or sub-economic amounts of gold (Bozkaya, 2001; Yilmaz, 2002; Oyman et al. 2003; Orgun et al. 2005; Bozkaya and Gokce, 2009; Yilmaz et al. 2010; Ozen and Arik, 2013; 2015; Imer et al. 2013; Bozkaya et al. 2014; Smith et al. 2014; Kumral et al. 2016).

Mineralization at Arapucandere, which was a base-metal deposit, resulted from episodic lithostatic–hydrostatic pressure variations (Bozkaya and Banks, 2015) within fault and fracture systems creating space for mineralization and providing a mechanism that induces massive ore deposition. Quartz is present as largely pre-ore coarse crystals and syn-to post ore finer-grained crystals. Different episodes of deposition for each type of quartz are evident indicating repeated influx of fluids. Sulphides such as sphalerite, galena and chalcopyrite, cut the coarser grained quartz and also show evidence of multiple periods of deposition. Pyrite is an early phase, occurring within the quartz that is cut by the other sulphides. The succession of sulphide minerals seems to follow the sequence pyrite, galena (1), chalcopyrite (1), sphalerite (1), galena (2), chalcopyrite (2), sphalerite (2).

This study uses material from the Arapucandere deposit in the Biga Peninsula which is typical of the deposits that were exploited for base-metals but also have variable amounts of gold. This deposit has the general characteristics of intermediate-sulphidation mineralization, and is similar to other deposits in this region. Almost all the deposits are hosted by Tertiary calc-alkaline (andesite, dacite, rhyodacite and rhyolite) and alkaline (olivine basalts) volcanic and volcano-clastic rocks, however at Arapucandere the base-metal deposit is vein-type, hosted by Palaeozoic metamorphic rocks and Permo-Triassic clastic rocks. The geological setting and characteristics of the mineralization and fluid inclusions have been described by Yucelay (1971; 1976); Atilqan (1977); Cagatay (1980); Cetinkaya et al. (1983); Anil (1984); Anil and Yaman (1985); Orgun et al. (2005); Bozkaya et al. (2008); Bozkaya (2011).

Previous work on Arapucandere by Bozkaya and Banks (2015) was related to veins containing sulphides where fluid inclusions indicated mineralization was precipitated from low to moderate salinity fluids. Other base-metal-gold deposits in the region also have a fluid

population that is of low salinity, c. 0-2 wt.% NaCl equiv. but may also have a separate fluid that has higher salinities of c. 8-10 wt.% NaCl equiv. The implication in these studies is that there was mixing between low and high salinity fluids, with the low salinity fluid having a meteoric origin (Oyman et al. 2003; Orgun et al. 2005; Unal et al. 2013; Yilmaz et al. 2013). Deposits that are primarily gold resources usually only show the presence of the low salinity fluid. The mixing hypothesis, when plotting salinity versus homogenization temperature, is an observational artefact based on the assumption that slightly cooler and low salinity fluids must be meteoric and has not been proven (Banks et al. 2016). A similar trend can be produced by boiling of a moderate salinity fluid. Isotope studies by Bozkaya et al. (2016) show that the fluids in the mineralizing systems are magmatic-dominated and variations in δD and $\delta^{18}O$ are the result of equilibration of magmatic fluids with different alteration minerals at different temperatures.

3. Materials and Methods

3.1 Quartz Vein Sample

In figure 1a. the photograph is of a mineralized vein sample from Arapucandere deposit on display in the Canakkale 18 Mart University's Earth Science Museum. Large euhedral quartz crystals occur after the deposition of high grade massive sulphides that were initially precipitated in the vein. The quartz crystals investigated in this study (fig. 1b) are not from this sample but they have the same context. They come from where the mineralized veins are hosted by the meta-diabase (within 100 m from the contact with the meta-sandstone), and have the same mineralogy and sequence of deposition as in figure 1a. ending with the euhedral quartz crystals. Samples were cut and polished both perpendicular and parallel to the c-axis to expose the full growth history. Crystals are typically 4-5 cm in length and show several pulses of growth.

3.2 Microthermometry

Microthermometric studies of the fluid inclusions was carried out using a Linkam THMS 600 heating-cooling stage in the University of Leeds. The temperature of phase changes for eutectic melting (Te), ice melting (Tm_{ice}) and homogenization to liquid or vapour (Th_L or Th_V) were recorded. Phase transitions below 0 ^{O}C are accurate to within $\pm$ 0.2 ^{O}C

based on calibration with pure CO_2 and H_2O standards, with a similar level of precision. Above 0 ^{O}C, accuracy was $\pm$ 2 ^{O}C based on the melting point of pure solids and synthetic fluid inclusions standards, with a precision of $\pm$ 1 ^{O}C. The ice-melting temperatures were converted to salinities using the equation of (Bodnar, 1993) and assuming the fluid composition is represented by the H_2O-NaCl system.

3.3 LA-ICP-MS of Fluid Inclusions and Quartz

The chemical analysis of individual inclusions, or individual inclusions within inclusions clusters was made by LA-ICP-MS using an Agilent 7500c mass spectrometer, combined with a Geolas ablation system at the University of Leeds. This system uses a Compex 103 ArF excimer laser producing a wavelength of 193 nm with an energy density typically 10 Jcm^{-2} at the sample surface. The operating frequency of the laser was 5 Hz with spot sizes of 25 μm and occasionally 50 μm, the main criteria being that the size was greater than that of the inclusions. The ablated material was transported from the ablation cell to an Agilent 7500c ICP-MS using 99.9999% He gas flowing at 2 ml min^{-1} into a cyclone mixer where it was combined with the Ar carrier gas flowing at 1.02 ml min^{-1}. The mixer prolongs the signal from the ablated inclusions and improves precision by increasing the number of cycles through the mass range of the selected elements and therefore the number of determinations of their ratio relative to Na. The instrument was operated in reaction cell mode using 2.5 ml min^{-1} 99.9999% H_2 gas to remove interferences from ^{40}Ar on ^{40}Ca and from ^{56}ArO on ^{56}Fe. For the elemental analysis of fluid inclusions, intensity ratios were converted to weight/weight ratios, relative to the internal standard element Na, using the NIST glass standard SRM-610 and the soda lime standard SRM-1412 for (for K/Na). The K/Na ratio of NIST 610 is 0.0047 which is distinctly different from the ratio in the fluid inclusion therefore, SRM 1412 with a K/Na ratio of 0.988 is closer to the values obtained from fluid inclusions. For the analysis of quartz, 50 μm diameter ablation spots were used and the elements determined against Si as the internal standard. NIST SRM-610 was used to check for instrumental drift, which was insignificant over each day's analysis. Integration of the standard and sample signals used the SILLS software package (Guillong et al. 2008). Full details of the analytical protocols and calibration of the instrument are presented in Allan et al. (2005). Particular attention was paid to ensuring any contamination was removed (Schloglova et al. 2007) and the samples were washed several times with 18.2 MΩ de-ionsed water. Areas of the quartz devoid of fluid inclusions were ablated for the same duration as for

the analysis of fluid inclusions, to determine if there was any contamination from the surface of the quartz or to detect if any Au-Ag particles were present in the quartz matrix. No contamination was detected and the very low concentration of Au and Ag determined in the quartz (figure 12) which is orders of magnitude less than when inclusions were ablated, shows there are no significant particles of Au-Ag in the matrix.

The elements determined in the fluid inclusions and quartz were ^{23}Na, ^{24}Mg, ^{39}K, ^{40}Ca, ^{55}Mn, ^{56}Fe, ^{63}Cu, ^{66}Zn, ^{88}Sr, ^{107}Ag, ^{137}Ba, ^{197}Au and ^{208}Pb each having a 10 ms count time. To obtain a better determination of the ^{107}Ag and ^{197}Au, a separate set of ablations determining only ^{23}Na, ^{39}K, ^{107}Ag, ^{197}Au and ^{29}Si with count times of 10 ms for ^{23}Na, ^{39}K and ^{29}Si, 20 ms for ^{107}Ag and 40 ms for ^{197}Au was performed. The increased counting time for Au was to reduce as much as possible the loss of signal from small Au particles. Each element is measured sequentially, but it is inevitable that regardless of the counting time for Au some particles will pass through the ICP-MS without being detected.

3.4 Electron Microscopy

Polished and carbon-coated (Lloyd, 1987) fluid inclusion wafers, were imaged using back scattered electron (BSE) atomic number (Z) contrast imaging on a FEI Quanta 650 scanning electron microscope (SEM) at the University of Leeds. Areas consisting of quartz with high concentrations of trace metals and mineral impurities were identified in BSE images via their large Z-contrast difference. Major and minor phases present were identified using an attached Oxford X-max 80 energy-dispersive X-ray spectrometer (EDS). Samples were also imaged simultaneously via cathodoluminescence (CL) using a KE Centaurus panchromatic CL detector, the final image being a mosaic of 2.5 mm squares.

4. Quartz Textures

4.1 Optical Microscopy

Quartz is the dominant gangue mineral in hydrothermal veins and exhibits a plethora of macroscopic textures related to the initial crystallization or re-crystallization (Adams, 1920; Sander and Black, 1988; Dong et al. 1995). The deposition of silica can be related to the saturation state with silica gels/colloids deposited from highly saturated solutions, then recrystallizing into a number of different textures depending on the conditions. Classification of the different textures can provided an understanding of the fluid conditions during and post mineralization and aid in defining the highest grade ore zones (Moncado et al. 2012).

Large (c. 5 cm) free growing euhedral quartz crystals are common at the Arapucandere deposit, with the crystals analysed here (sample from the 5th vein in the meta-diabase), having been attached to the sulphide mineralized meta-diabase which acts as the wall rock. (fig. 1a). Only where the quartz crystals were attached to the wall rock are there very minor amounts of sphalerite and galena. No sulphides are present during growth of the rest of the crystal (a summary of the mineralogy and petrography of the mineralization at the deposit and the samples used in this study are presented in Bozkaya and Banks (2015). The crystals show discrete periods of growth, from separate pulses of fluid, and sections parallel to the c-axes show evidence of a number of quartz overgrowths, often marked by variable numbers of fluid inclusion that align perpendicular to the crystal faces. The intensity of fluid inclusion trapping may be quite low or extremely high as shown in figure 2 a-c where the inclusions are marked by the black lines which in figure 2c are observed to go in different directions as they are on different crystal faces with different orientations. In figure 2d, overgrowths on a perfectly euhedral quartz crystal, that exhibits sector zoning, have areas of high and low density of fluid inclusion trapping. In crossed polarized light the overgrowths have a striated pattern of light and dark bands. The dark areas are where fluid inclusions are present and light areas are quartz. The quartz has grown as a series of closely spaced fibres, trapping the fluid inclusions between the fibres resulting in the long elongated fluid inclusions and trails that are observed in figure 4a. Similar growth textures in euhedral quartz are also present in many other deposits in western Turkey and are a common feature in epithermal deposits in general (Bodnar et al. 1985).

Fibrous veins are common in metamorphic quartz veins where repeated crack and seal events play an important part in their formation (Urai et al. 1991). Van de Kerkhof and Hein (2001) also show examples of fibrous textures in euhedral quartz crystals that trapped primary fluid inclusions during crack seal events. However, in this study the fibrous quartz is related to the growth of quartz in a free fluid environment without any tectonic or deformational triggers. This type of fibrous growth is typical of fast growth and can be seen in quartz overgrowths produced in hydrothermal cell experiments (Larryn Diamond *pers comm.*). White and Corwin (1961) showed in hydrothermal experiments that chalcedony and fibrous quartz were rapidly produced but that the chalcedony converted to quartz within 96 hours. In the conversion, the fibrous quartz precipitates with sub-microscopic holes because of the negative volume change. It also requires a pre-existing surface from which the fibrous quartz would form.

4.2 Cathodoluminescence

Scanning electron microscope cathodoluminescence (SEM-CL) imaging (Rusk and Reed, 2002; Gotze, 2009; Lehmann et al. 2009; Frelinger et al. 2015) shows in greater detail the quartz textures during crystal growth. Individual growth pulses and the banding within these arising from lattice effects, trace element incorporation and twinning can be recognized and may reflect the variability of the fluid pressure, temperature and composition of the fluid during quartz crystal growth. Two SEM-CL maps (supplementary figures) of quartz crystals cut perpendicular to the c-axis generally display regular micron-sized growth bands within the period of crystal growth for individual fluid pulses. However, there are instances where different growth textures are observed. Figures 3 a, b show one of these crystals as a 250 μm thick, doubly polished wafer that was used for fluid inclusion studies, which when illuminated with normal visible light from above (fig. 3a) shows areas of trapped fluid inclusions as light-coloured regions that correspond with the dark areas in the CL image (fig. 3b). The CL technique was used by Boiron et al. (1992) and Van den Kerkhoff and Hein (2001) to show how fluid inclusions could be related to domains in quartz. Lambrecht and Diamond (2014) also showed how the CL image can identify fluid inclusions, but they also determined the CL image is larger than the optical image of inclusions due to dissolution and recrystallization which changes the composition of the re-deposited quartz. In this study we have used the CL images of the fluid inclusions and fluid inclusion trails to determine their relation to the growing quartz crystal. Trapping of fluid inclusions can occur at defect sites on the growing crystal face and by rapid growth, but here primary fluid inclusions were not trapped in the majority of the growing crystal indicating that, for most of the time, growth was slow and the crystal faces were defect free.

In the CL images, all areas of fluid inclusions are black and easily distinguished from the black crystallographic boundaries (Fig 4c). At specific locations throughout the crystal, parallel dark bands of fluid inclusions, some of which were opened during polishing due to their large size, occur perpendicular to the growth faces of the quartz crystals as dense accumulations (fig. 4 a, b). The number of trapped fluid inclusions is variable, but they are particularly numerous towards the termination of the crystal growth. The reason for the sudden dense accumulation of fluid inclusions is unclear, but is most likely due to sudden variations in the fluid pressure. The orientation of fluid inclusions perpendicular to crystal faces is frequently observed in growth bands of quartz from epithermal and other styles of mineralization (Bodnar et al. 1985). As the quartz crystals have grown in free space, in a vein,

the trapping of fluid inclusions in these linear arrays cannot be the result of mechanical deformation. As shown (fig. 2 d, e) fluid inclusions were trapped in the space resulting from the fast growth of fibrous quartz.

The CL images (fig.4) illustrate different episodes of trapping fluid inclusions which are likely due to sudden physical events. Elongate trails of fluid inclusions appear to cut across growth zones and terminate at the first of two distinctive crystal boundaries (fig.4a). Between these boundaries the black area defines where fluid inclusions have been trapped as clusters of multiple inclusions. The area of most intensive trapping of linear arrays of fluid inclusions is (fig.4b) near the termination of quartz crystal, also occurring on the opposite side of the crystal on a different crystal face (fig. 3b) and would have been present on all six faces of the quartz crystal. The inclusion trails can be seen to originate from distinct crystal faces and appear to cut across numerous distinct growth bands (fig. 4a). Fluid inclusions were trapped between the growing fibrous quartz (fig. 2e) but the lack of luminescence from the fibrous quartz, contrasts with the dark fluid inclusion areas, giving the impression that the fluid inclusions cut the quartz growth bands. However, the fluid inclusions are clearly primary being trapped as the quartz grew.

Trapping of secondary inclusions can easily be identified with CL as the crystal faces are more obvious than with optical microscopy (fig. 4c). The termination of a period of euhedral quartz growth is marked by the black lineation outlining the crystal faces. Further growth continued, but it is clear that the growth textures are different. Within the euhedral quartz (Qz-a), growth zones that are parallel the crystal faces occur, but these are absent in the next generation of quartz (Qz-b). Here the texture of the quartz appears as series of elongate, almost comb like, individual crystals where banding related to the crystalline structure is absent. Within the earlier euhedral quartz (Qz-a) there is an obvious black fluid inclusion trail that terminates on both of the external growth faces of the quartz. It does not extend into the next generation of quartz (Qz-b) and so these can be classed as pseudosecondary fluid inclusions that represent the fluid which precipitated the next generation of quartz. A part of this inclusion trail is shown (fig. 5f), where the inclusions are seen to be dominated by vapour (V-rich) with very little aqueous fluid.

There is a zone at the base of the crystal (fig 4d), where the initial growth of quartz started on the meta-diabase wall rock. Well-formed euhedral quartz, with numerous growth zones, grew first and these contain only a few primary liquid-vapour (L-V) inclusions. Above

this the quartz has an intensely mottled appearance due to the dark patches which represent the chaotic trapping of a very large number of all sizes of predominantly L-V inclusions, that have variable L/V ratios, and also a few V-rich inclusions. This area is terminated by some colloform banding before the resumption of normal crystal growth.

5. Results

5.1 Fluid Inclusions

Examples of the petrography and types of inclusions found are shown in figure 5. Primary inclusions are located in zones where, predominantly L-V, fluid inclusions are trapped in significant numbers in linear arrays originating from existing crystal faces. These are typically between 20 μm and 100 μm in size (fig. 5a). V-rich inclusions are much less common, but may occur with L-V inclusions in the same linear trails. V-rich inclusions frequently occur in fractures that appear to be peseudosecondary (fig. 4c, 5f), where trails originate from the outer surface of quartz crystal, however they may also be of secondary origin. There are examples of clear secondary fluid inclusions as seen in CL (fig. 4c) where a trail of inclusions starts in the later quartz growth (Qz-b) and cuts the outer face of the euhedral crystal and through numerous growth bands in Qz-a. Examples of these smaller, c. 10 μm sized L-V inclusions are seen (fig. 5f) intersecting the pseudosecondary trail of V-rich inclusions. The number of secondary and pseudosecondary inclusions is much lower than primary inclusions.

Primary fluid inclusions in clusters (fig. 5b), are an example of the inclusions that are observed between the two distinctive growth bands in figure 4a and also occur randomly throughout the quartz crystal. The inclusions (fig. 5a, b) can have variable L/V ratios within the same cluster that are visually similar to the variation of L/V ratios in the linear trails of inclusions. This, combined with the presence of V-rich inclusions (fig. 5d, e) that homogenize to vapour, would be consistent with trapping of a fluid that has boiled. There are a significant number of inclusions that contain a solid (fig. 5b, c) that may be illite, as this has been shown to precipitate in epithermal systems in areas where fluids have boiled (Moncado et al. 2012). Secondary L-V inclusions all have a consistent L/V ratio and are generally smaller in size compared to primary inclusions.

Some 29 areas of fluid inclusions, covering most of the crystal, have had the homogenization temperature (Th) and salinity determined by microthermometry. The locations of these areas are shown in figure 3b (and supplementary figures), along with the

average salinity of the inclusions measured in each area. All of the Th values are between 270 and 340 ^{O}C, regardless of the salinity of the inclusions, with a Gaussian distribution and a modal value of c. 305 ^{O}C (fig. 6a). The salinity does not vary within individual areas, but may do so between different areas. The majority of the salinities are low c. < 2 wt.% NaCl equiv. but a small number of areas, where the inclusions appear to be secondary, have salinities up to c. 8 wt.% NaCl equiv. The distribution of salinities is (fig. 6b) essentially bimodal with groups centred around 4.5 and 1 wt.% NaCl equiv. There is a tail of inclusions that go to higher salinities but these come from inclusions that are secondary in origin. The lack of any clear relation between salinity and Th is evident (fig.7). Although V-rich inclusions can be large > 30 μm (fig 5e), the small amount of liquid present made determination of their salinity impossible. They do exist in inclusion clusters together with, what appear to be V-only inclusions (fig. 5d, f), and inclusions with variable L/V ratios (fig. 5a, b). Overall the measured Th values of V-rich inclusions (homogenize to vapor) are consistent with the Th values of L-V inclusions that (homogenize to liquid) and so in some areas homogenization to both liquid and vapour occurs, indicating there was boiling. (Microthermometry data of all the inclusions measured is included in the microthermometry data Excel file in supplementary material).

5.2 Particulate Au-Ag in Fluid Inclusions

Due to their large size many fluid inclusions were opened during polishing of wafers which were used both for fluid inclusions and CL. In the CL images, bright mineral/solid inclusions were observed in open fluid inclusions. Two open inclusions of c. 50 μm size are shown in the back scattered electron (BSE) image figure 8a, where the brightness is relative to the atomic number of the main element (brightness increases with increasing atomic number). In both inclusions (fig. 8a) and in almost all open inclusions imaged by BSE, several sub-micron gold particles can be seen (fig. 8b) with the largest being c. 1 μm in size, but are commonly smaller than this. These are attached to the walls of the inclusion or (fig. 8b) on calcite or baryte crystals. Gold particles can be distinguished as they are always rounded and are the brightest objects, for example in figure 8b where two of the brightest rounded grains are attached to a more rectangular, less bright, baryte. With the largest gold inclusions it was possible to use BSE element mapping to obtain qualitative compositional data that showed there was silver, copper and occasionally mercury in addition to gold (fig. 8c). Other small crystals, which can be numerous, are present in the open fluid inclusions and energy dispersive spectroscopy (EDS) identified these as pyrite, baryte, galena, sphalerite and

calcite (spectra are presented in supplementary data). The actual number of gold particles and other minerals in the fluid inclusions is unclear as an unknown number would have been lost when the inclusions were opened during polishing. In greater magnification of a different inclusion (fig. 9a), numerous sub-micron gold particles, some as small as 100 nm can be observed in the BSE image. These are attached to the surface of semi-crystalline calcite (fig. 9b) that coats the inner surface of the fluid inclusions. All the gold particles in the large liquid-vapour inclusions are too small to have been observed with an optical microscope. The presence of gold particles in the inclusions could be the result of precipitation elsewhere and transportation and trapping with the fluid, or they precipitated from solution once the fluid inclusions were trapped. As with other solids it is likely that particulate gold was lost when the inclusions were opened, which is consistent with LA-ICP-MS analyses that show, when ablating open inclusions, they generally have lower Au and Ag concentrations compared to ablation of unopened ones. As far as we are aware, this is the first time that particles of gold have been observed in fluid inclusions.

In addition the inclusions also contain variable numbers of different minerals as shown in the composite element map of a large inclusion (fig. 10). A semi-crystalline precipitate of calcite coats the inner surface of the inclusion with discrete areas of high concentrations of Na, Mg, Ca, Al, Fe and Ba. The distribution of S coincides with Ca. Spectra of different mineral phases were obtained (shown in supplementary figures) confirming the presence of calcite, baryte, pyrite, galena, sphalerite.

5.3 LA-ICP-MS Analyses

A total of 146 fluid inclusions from 9 of the lower salinity areas, one higher salinity area and one trail of vapour dominant inclusions, where salinity could not be determined due to the small volume of liquid, were analysed by LA-ICP-MS. The different areas where inclusions were ablated and analysed by LA-ICP-MS are indicated in figure 3b (yellow colour). The average analyses are calculated as concentrations in ppm (Table 1), using the salinities determined by microthermometry. The salinity used for the V-rich inclusions was the average of all the low salinity inclusions measured in the different areas on the assumption the fluid in the V-rich inclusions has either condensed from vapour on cooling or the vapour carried a small amount of the low salinity liquid when it boiled. In either case the salinity should be similar.

The signals for the sequential ablation of 3 fluid inclusions are shown in figure 11a. The duration of the Na and K signal above that of the background signal signifies the time the laser was ablating the inclusion, usually around 10 - 12 seconds. The laser was ablating for 200 pulses at a rate of 5 Hz and thus the signal for Si lasts for 40 seconds. As the laser ablates deeper into the quartz it is possible other inclusions can be opened, but here it can be seen no other inclusions were intersected during this 40 second period. The signal for Au and Ag is distinctive at over 100 times that of the background, which is only 0 or 1 counts, and is only observed during the same period as the Na and K signal from the liquid in the inclusion is present. There is no Au or Ag signal as the laser continues to ablate the quartz matrix and thus we can be certain that these are only in the fluid inclusion. As shown (fig. 8), Au and Ag have been observed as sub-micron particles in the fluid inclusions and we can distinguish between Au and Ag that is in solution and Au and Ag that are present as particles from the ablation signal profile. The normal signal from elements in fluid inclusions is asymmetric, with a rapid increase as the inclusion is opened followed by a slow decrease to the background. In general the signal for the different elements in solution will be approximately parallel to each other as seen (fig. 11a, b) for Na and K. However, in both figures the signal for Au is not smooth and asymmetric consisting of a number of spikes. This is also true for Ag signal which shows a close similarity to the signal for Au. We interpret this to confirm that Au and Ag are present as particles in the fluid inclusions. As the ICP-MS measures each isotope sequentially, when particulate gold is ablated its signal will not be recorded if the ICP-MS is measuring another isotope at that time. Therefore, not all fluid inclusions that are ablated will show the presence of gold particles or record the presence of all the particles present in the fluid inclusions.

The analyses of fluid inclusions (Table 1) are dominated by Na and the other alkali and alkaline earth elements with Na/K wt./wt. ratios of (2.0 to 4.7 average 3.3, one value 6.3) and Na/Ca ratios of (2.2 to 3.7 average 2.9) being generally similar between the different areas analysed. The Na/Ca ratio of the inclusions in the vapour trail is however, distinctly different with a ratio of 22. The majority of Na/Mg wt./wt. ratios for the different areas analysed are also similar (4 to 11.4 average 8.4), but in two instances the values of 24 are likely due to the very small Mg intensities from the fluid inclusions. The Na/Mg wt./wt. ratio of 300 for the V-rich inclusions is however, significantly different. Overall the major element composition would be consistent with the fluid inclusions originating from the same source. The other elements (except Ag and Au) are present in low concentrations of 10's to a few

100's ppm in the fluid inclusions. (A summary of the average wt/wt ratios, standard deviation, relative standard deviation, concentration and the method of calculation to estimate the concentration is given in the supplementary LA-ICP-MS Excel file).

The relative standard deviation for the alkali and alkaline earth elements and trace elements, relative to the internal standard element Na, is somewhat higher than is normally obtained when analysing fluid inclusions. The higher than normal reproducibility is due to many elements being present in the inclusions as mineral precipitates (fig. 10) as well as in solution. The LA-ICP-MS data was processed to remove excessively large element/Na ratios (from the ablation of minerals) but the effect may still be present at a lower level. The average concentrations of all the analysed inclusions for Au and Ag are a few 10's of ppm, with one exception of 233 ppm. However, the reproducibility of analyses for Au and Ag is well over 100% due to these elements being present as particles in the fluid inclusions and not dissolved in solution (spikey signals in figure 11). Part of the variability in concentration is due to the inevitability that the sequential measurement of isotopes will result in an unknown number of particles passing through the ICP-MS without being measured, hence the reduction in the precision of the average analyses. In addition if the particles were precipitated before entrapment, the number trapped in the fluid inclusions could vary immensely between different fluid inclusions. The range in Au and Ag analyses can be seen in figure 12, where Ag-Au pairs are plotted and show that there is an almost 3 orders of magnitude range in measured concentrations for Au and Ag. The concentrations are from ablation of single unopened fluid inclusions and are all in excess of the detection limits shown for analyses of Au and Ag in fluid inclusions. Using this data the average concentration for Ag is 32 ppm and Au 41 ppm, but as not all of the Au-Ag particles will have been detected by the ICP-MS we suggest the true concentration of Au and Ag in the fluid inclusions may be towards the higher end of values recorded, c. 100 ppm.

A number of LA-ICP-MS analysis were made on the quartz matrix, but the Au and Ag concentrations are well below 0.5 ppm, confirming all the Au and Ag we have detected resides in the fluid inclusions. The lack of Au and Ag when ablating the quartz also shows there is no surface contamination affecting the analyses of Au-Ag despite the fluid inclusions being close to the surface

6. Discussion

The initial object of this study was to examine how the growth textures of the euhedral quartz crystals changed with time. The whole crystals were imaged with SEM cathodoluminescence as similar work was shown by Rusk and Reed (2002); Gotze (2009); Landtwing et al. (2010); Lambrecht and Diamond (2014) and Rottier et al. (2018) as a means of linking growth textures and the conditions during growth. However, it was apparent that as well as textural information the presence of numerous areas of fluid inclusions, preserved at different periods of quartz growth, provided an opportunity to determine the pressure-temperature-composition (P-T-x) of the hydrothermal fluids as the quartz crystal grew. The large euhedral crystal, cut perpendicular to the c-axis (fig. 3a, b), shows numerous periods where inclusions were trapped during growth of the quartz overgrowths and as such are primary fluid inclusions that reflect the P-T-x at that time.

The vein sample (fig. 1a) shows three different styles of mineral precipitation, the deposition of massive essentially mono-mineralic sulphides, sulphide deposition in a breccia system, both in the meta-diabase host rock, and the growth of large euhedral quartz crystals in an open vein. The first two imply a rapid deposition in a high energy environment while the growth of euhedral quartz (fig. 2b), has taken place in conditions close to equilibrium growth. From this study and previous fluid inclusion work at Arapucandere (Orgun et al., 2009; Bozkaya and Banks, 2015) the fluid salinity was found to be very low c. 1-2 wt.% equiv. in quartz hosted inclusion. In general, fluid inclusion studies from other epithermal deposits in western Turkey also show a range of salinities in base-metal ± Au deposits, but deposits that are Au resources generally only have fluid inclusions dominated by the lower salinities. In all cases the temperature of the earliest fluids was approximately the same c. 280 to 350 ^{O}C. The interpretation that the low salinity fluids were of meteoric origin and these diluted the higher salinity ore-fluids causing the deposition of ore is unproven, however, Bozkaya et al. (2016) show that all the fluids have a magmatic origin and if meteoric water was involved its contribution was probably minimal.

The Th and salinity of inclusions measured here are consistent with the higher temperature group of inclusions (Th between 270 and 350 ^{O}C and salinities c. 1 wt.% NaCl equiv) in the previous study of Bozkaya and Banks (2016) and other deposits in the Biga Peninsula (see Bozkaya et al., this issue). However, here we have not identified a lower temperature group of inclusions that was present in previous studies and signifies a separate, later, fluid pulse. The evidence of boiling from trapping L-V and V-rich inclusions that, on average, homogenise to both liquid and vapour at c. 305 ^{O}C, would at hydrostatic conditions,

indicate a depth of some 1600 m which is unreasonable as the veins are close to the surface and there has not been erosion of over 1000 m. Fluid inclusions trapped within the same assemblage should have similar characteristics, but here the Th of the inclusions varies by some 70 ^{O}C, which is much greater than any measurement error. Bozkaya and Banks (2016) showed how a similar range of Th values and boiling were consistent with pressure decreasing from lithostatic to hydrostatic at a depth of c. 600 m which approximates the depth of the samples and mineralization at the deposit. As the vein initially opens, the pressure in the space created is very low, but as hydrothermal fluid flows into the open vein the pressure will rise to at least hydrostatic, but could be higher if there is still a lithostatic pressure component. The fluid will expand and lose temperature by adiabatic expansion and so the first inclusions trapped will have the lowest Th. As more fluid flows in, the pressure will rise and the lowering of temperature will decrease with time so the Th of later trapped inclusions will be higher. Hence fluid inclusions trapped from the same pulse of fluid can record a range of Th values. We suggest that throughout the growth of crystals in this vein there were several periods of pressure variation and influx of new fluid leading to new overgrowths of quartz on previously formed crystals, which is shown clearly the by CL-images (figs. 3, 4).

If the majority of Au and Ag was transported as particles, then the number of particles trapped in fluid inclusions may be random. The concentrations of both Au and Ag range over two to three orders of magnitude (fig. 12), even from inclusions that are analysed from the same area. As previously mentioned the LA-ICP-MS transient signal for these elements (fig. 11) consists of numerous spikes indicating the signal comes primarily from solids, although some Au and Ag will be in solution at the saturation levels for the salinity and the room temperature. Other elements have a smooth ablation profile that indicates they are in solution. There are two options for the large variation in Au and Ag concentration and its particulate nature. Either the Au-Ag particles are true daughter crystals and have precipitated from the fluid in the inclusions as it cooled from c. 300 ^{O}C to room temperature, or the Au-Ag particles were trapped between quartz fibres and are therefore accidentally trapped. In the former case, variations in the concentrations may be analytical as the ICP-MS measures the elements selected sequentially and it is likely that some of the Au-Ag particles would pass through the instrument when the mass spectrometer was measuring other elements. However, even reducing the elements measured and increasing the dwell time for Ag and Au with a reduction in the cycle time for the mass spectrometer to measure all elements and return to the start for another pass, did not significantly reduce the large variation in the measured Au-

Ag concentrations. The alternative is that the Au-Ag particles were not precipitated from the liquid in the fluid inclusions, but were, in fact, accidentally trapped having been carried by a low density vapour which then condensed to form the low salinity fluid in the fluid inclusions. In this case the same analytical issues would exist but the variability in measured concentrations would be compounded by the heterogeneous trapping of particles. Our contention is that Au-Ag particles were precipitated from solution in a deeper part of the hydrothermal system and carried as colloids or larger, but still sub-micron sized particles, by the fluid (vapour or liquid phase) as it ascended to shallower levels and the epithermal environment.

If gold had precipitated from the fluid in the trapped inclusions, then the range of measured concentrations covering 3 orders of magnitude is too large to be accounted for by the analytical error induced by not measuring all the Au-Ag particles. In addition the concentrations determined here are substantially above any reported analyses, or of any theoretical concentrations (Gammons and Williams-Jones, 1997; Hurtig and Williams-Jones, 2015). However, experimental results of liquid vapour partitioning (Zajacz et al. 2017) at closer to magmatic temperatures show the vapour phase can attain concentrations of a few 10's ppm Au but still below the values determined in this study. Therefore, the presence of Au-Ag particles is most probably due to heterogeneous trapping in the fluid inclusions, having first been precipitated elsewhere in the mineralizing system.

The FI's are large L-V, generally elongate and may reach 100 μm in length in the upper intense zone of trapping, but are smaller in other areas, and over the length of the crystal the salinity and homogenisation temperature (Th) shows little variation, Th is between 280 and 350 ^{O}C and salinity, in two groups between c. 0 and 3 and 3 and 5 wt.% NaCl equiv. These salinities are consistent with the condensation of magmatic vapour to produce low salinity fluids in epithermal systems (Heinrich et al. 2004; Heinrich, 2005; Landtwing et al. 2010; Berger and Henley, 2011; Henley and Berger, 2011; Rottier et al. 2018). Gold is preferentially concentrated into the vapour phase when the magmatic fluid separates into the high salinity brines and low salinity vapor (Hurtig and Williams-Jones, 2015: Ulrich et al. 1999). In general, metal concentrations may reach 1000's ppm in the brine with gold at the c. 5-10 ppm level. In the vapour phase, Au concentrations as high as 10ppm have been reported, but it is usually lower. However, in terms of mass transport the vapour phase is volumetrically more important. LA-ICP-MS was used to analyse the composition of fluid inclusions, however, the presence of other solids, calcite, baryte, galena, sphalerite, pyrite,

chalcopyrite and gold, adversely influences the analyses of what should be inclusions containing only liquid and vapour (fig. 10). On a weight ratio basis relative to Na, which should be the dominant cation, the measured cations of the previously mentioned minerals are quite variable and in a number of instances much too high. Some inclusions have Ca, Ba, Fe etc. at concentrations greater than Na.

The solubility of Au determined in experimental studies is not close to values measured in the fluid inclusions and is much lower than previously determined values in prophyry and epithermal deposits, which are usually less than 10 ppm. Sanchez-Alfaro et al. (2016) show that in present day geothermal fluids a small pressure drop of 10 bars is enough to precipitate 95% of the gold from solutions that carry ppb levels of Au. Previously (Bozkaya and Banks, 2015), showed that the fluid inclusions in the Arapucandere veins recorded a pressure drop of some 100 bars going from close to lithostatic pressure to close to hydrostatic pressure, clearly enough to precipitate Au from the hydrothermal fluids. This may be due to deep over-pressured fluids exceeding the confining pressure or perhaps due to earthquake fracturing (Sibson, 1987; Sibson et al., 1988; Wilkinson and Johnson, 1996; Weatherly and Henley, 2013; Guluz, et al. 2018).

Analysis of Au and Ag in quartz matrix (fig. 6), where there are no fluid inclusions, shows the concentrations are c. 0.1 ppm which is close to the limit of detection. Therefore, Au and Ag were either not present in the fluids when the bulk of large euhedral quartz crystals were being precipitated, or was not precipitated and trapped. The high concentrations only occur where the quartz was growing as a series of fibres with fluid-filled spaces between them (fig. 2).

As Pb, Zn and Cu require high concentrations of chloride to transport them in appreciable concentrations (Seward and Barnes, 1997), it is highly unlikely that the low salinity fluids were also responsible for their transport. The sulphides precipitated in the deposit can be massive (fig. 1a), and in the sample we have studied have precipitated prior to the deposition of the quartz, which was the final mineral precipitating in the veins. However, we have recorded a higher salinity fluid was present episodically, but mainly as secondary inclusions (fig. 3b, 7). The greater availability of chloride complexing would be consistent with what would be required to transport larger quantities of base-metals in solution. This same scenario of cyclic mixing of low salinity magmatic fluid with higher salinity magmatic brines has been reported by Rottier et al. (2018) at the Cerro de Pasco deposit. In Table 1, the

LA-ICP-MS analyses of the higher salinity fluid inclusions show these contain significant concentrations of Cu (817 ppm), Zn (629 ppm) and Pb (210 ppm) which are higher than the average values of these metals in the lower salinity fluid. The increased concentration of the metals is more than can be accounted for by the differences in the salinity of the fluids. However, the opposite applies to the concentration of Au which has a low concentration in the high salinity fluids and a higher concentration in the low salinity fluid inclusions. We suggest this shows that in the low salinity fluid there was a greater concentration of reduced sulphur. Although we have not measured this directly, it can be inferred from the SEM element map (fig. 10) which shows the inside of the open fluid inclusions has a coating of an S-phase and the presence of baryte crystals. Our interpretation is that the low salinity fluid inclusions represent a low density vapour that separated from the higher salinity magmatic fluid and has condensed to a higher density liquid on cooling to a temperature where the vapour had to condense, analogous to the Dew Point (Heinrich et al. 2004).

7. Conclusions

The suggestion that gold can be transported as colloids has been proposed for some time (Herrington and Wilkinson, 1993; Saunders, 1990; 2012) as a means of transporting gold at elevated concentrations greater than is possible in solution. Although there are other constraints on forming giant epithermal gold deposits (Richards, 2013) “bonanza” grades (Saunders and Schoenley, 1995; Saunders, 2012) are often associated with the observation of colloidal gold in the ore veins. Direct evidence of gold colloids in hydrothermal fluids, was first reported by Garman et al. (2018) in the black smoker fluids from the Lau Basin that had boiled and cooled. Our observation, for the first time, of sub-micron gold particles being carried in a mineralizing fluid, and trapped in fluid inclusions, is consistent with a link to boiling.

It is clear that the Au-Ag particles did not precipitate from the fluid once it was trapped as fluid inclusions. The heterogeneity of the LA-ICP-MS analyses and the high concentration of Au and Ag, which can exceed the concentrations of the alkali and alkaline earth elements, that are normally most dominant in hydrothermal fluids, is not feasible. Instead we propose that the particulates trapped in the inclusions are the consequence of fluid boiling elsewhere in the mineralizing system and have been accidentally trapped. The fluids and solids were trapped between rapidly growing fibrous quartz, which would create

structures similar to fluid-filled tubes, during periods when the fluid was supersaturated with respect to quartz. As pulses of hot low salinity fluid and/or vapour ascended from deeper in the mineralizing system, these cooled due to adiabatic expansion, which led to a decrease in silica solubility as well as that of the metals in solution. Reduction in pressure leading to boiling is also likely to have been a major factor in precipitating different minerals. The calcite coating of the inner walls of the inclusions together with the precipitation of sulphates and sulphides is reminiscent of the associations observed in vein systems with boiling zones. In the quartz crystals studied, the fluid inclusions provide evidence of pressure transitions from close to lithostatic to close to hydrostatic, and the presence of flashed fluids (fluids which on rapid pressure drop instantaneously convert to low density vapour) indicates, on some occasions, there were periods of transient sub-hydrostatic pressures. Fluids were boiling during these pressure fluctuations and cooled to lower temperatures which is also likely to be the reason for the precipitation of the more massive sulphide ores in other parts of the vein systems.

Numerous examples of base-metal and Au, or Au dominated deposits are present in the Biga Peninsula of NW Turkey (Bozkaya et. al. 2019, in revision, this volume). The fluid inclusion characteristics of those Au-deposits are similar to the low salinity fluids in this study. Other deposits that are base-metal resources, contain fluid inclusions with higher salinities, but almost all have the same low salinity fluid as at Arapucandere. The previous interpretation that this low salinity fluid had a meteoric origin is clearly incorrect as we have shown. This is most likely a condensed low density vapour or low salinity fluid which separated from more saline magmatic fluids at depth expanding to cooler shallower levels. The presence of particulate gold at high concentrations in these fluids shows their importance in the mineralizing process as they appear to be the main transporter of gold. Thus, whilst the Arapucandere deposit is a minor one, the direct observation and transportation of Au and Ag in the form of nano-particles, and the high concentrations possible, is a significant result with implications for porphyry and epithermal mineralization.

Acknowledgements

The authors thank Larryn Diamond for his helpful comments which led to a better understanding of the processes presented in this paper. Richard Walshaw's technical expertise greatly enhanced the quality of the SEM and CL imaging. Antonin Richard and an

anonymous reviewer are thanked for their diligent reviews that improved the paper. Ibrahim Uysal is thanked for comments and his editorial handling of the paper.

References

Adams, S.F., 1920. A microscopic study of vein quartz. Econ. Geol. 15, 623-664.

Allan, M.M., Tardley, B.W.D., Forbes, L.J., Shmulovich, K.I., Banks, D.A., Shepherd, T.J. 2005. Validation of LA-ICP-MS fluid inclusion analysis with synthetic fluid inclusions. American Mineralogist, 90, 1767-1775.

Anil, M., 1984. Genesis of the Pb–Zn–Cu mineralization and relations with Tertiary volcanism in Yenice area (Arapuçandere–Kurttasi–Sofular and Kalkim–Handeresi). Chamb. Geol. Eng. Turk. 20, 17–30.

Anil, M., Yaman, S., 1985. Fluid inclusions studies on the Arapuçandere (Yenice-Çanakkale) Pb–Zn mineralizations. Bull. Earth Sci. Appl. Res. Cent. Hacet. Univ. 12, 81–91.

Atilqan, I., 1977. The conditions and origin of Biga Peninsula Pb-sulphosalts. Bull. Inst. Earth Sci. Istanbul Univ. 1-2, 53–76.

Banks, D.A., Bozkaya, G., Bozkaya, O., 2017. Comment on "Origin and evolution of hydrothermal fluids in epithermal Pb-Zn-Cu+Au+Ag deposits at Koru and Tesbihdere mining districts, Canakkale, Biga Peninsula, NW Turkey" Ore Geology Reviews, 86, 971-976.

Benning, L.G., Seward, T.M., 1996. Hydrosulphide complexing of Au(I) in hydrothermal solutions from 150-400^{O}. Geochim. Cosmochim. Acta 60, 1849-1871.

Berger, B.R., Henley, R.W., 2011. Magmatic-vapor expansion and the formation of high-sulphidation gold deposits: Structural controls on hydrothermal alteration and ore mineralization. Ore Geology Reviews, 39, 75-90.

Bertrand, G., Guillou-Frottier, L., Loiselet, C., 2014. Distribution of porphyry copper deposits along the western Tethyan and Andean subduction zones: insights from a paleotectonic approach, Ore Geology Reviews, 60, 174-190.

Bodnar, R.J, Reynolds, T.J., Kuehn, C.A. 1985. Fluid-inclusion systematics in epithermal systems. Reviews in Economic Geology Vol. 2, Geology and Geochemistry of Epithermal Systems. B.R. Berger and P.M. Bethke Eds. Ch. 5, 73-97.

Bodnar, R.J., 1993. Revised equation and table for determining the freezing point depression of H_2O-NaCl solutions. Geochimica et Cosmochimica Acta 57, 683-684.

Boiron, M.C., Essarraj, S., Sellier, E., Cathelineau, M., Lespinasse, M., Poty, B., 1992. Identification of fluid inclusions in relation to their host microstructural domains in quartz by cathodoluminescence. Geochimica et Cosmochimica Acta, 56(1) 175-185.

Bozkaya, G., Gokce, A., Grassineau, N.V., 2008. Fluid-inclusion and stable-isotope characteristics of the Arapuçandere Pb–Zn–Cu Deposits, NW Turkey. Int. Geol. Rev. 50, 848–862.

Bozkaya, G., 2001. Geology of Koru (Canakkle) barite bearing lead-zinc deposits. PhD Thesis, University of Cumhuriyet, 126 pp (unpublished).

Bozkaya, G., Gokce, A., 2009. Lead and sulfur isotope studies of the Koru (Canakkale, Turkey) lead-zinc deposit. Turkish Journal of Earth Sciences, 18, 127-137.

Bozkaya, G., 2011. Sulfur-and lead-isotope geochemistry of the Arapuçandere (Karaköy-Yenice, Çanakkale) Pb–Zn–Cu deposit, Biga Peninsula, NW Turkey. Int. Geol. Rev. 53, 116–129.

Bozkaya, G., Banks, D.A., Ozbas, F., Wallington, J., 2014. Fluid processes in the Tesbihdere base-metal-Au deposit: Implications for epithermal mineralization in the Biga Peninsula, NW Turkey, Central European Journal of Geosciences, 6, 148-169.

Bozkaya, G. and Banks, D.A., 2015a Physico-chemical controls on ore deposition in the Arapucandere Pb-Zn-Cu-precious metal deposit, Biga Peninsula, NW Turkey. *Ore Geology Reviews*, 66, 65-81.

Bozkaya, G., Banks, D.A., 2015b. The importance of supersaturated silica deposition for base-metal Au-Ag mineralization in western Turkey. Turkish Journal of Earth Sciences. 24, 99-110.

Bozkaya, O., Bozkaya, G., Uysal, I.T., Banks, D.A., 2016. Illite occurrences related to volcanic-hosted hydrothermal mineralization in the Biga Peninsula, NW Turkey: Implications for the age and origin of fluids. Ore Geology Reviews, 76, 35-51.

Bozkaya, G., Bozkaya,O., Banks, D.A., Gokce, A., 2019. P-T-X constraints on the Koru epithermal base-metal (±Au) deposit, Biga Peninsula, NW Turkey. Ore Geology Reviews, (in revision).

Cagatay, A., 1980. Geology and mineralogy of western Anatolian lead–zinc deposits and some comments about their genesis. Bull. Geol. Soc. Turk. 23, 119–132.

Canet, C., Franco, S.I., Prol-Ledsma, R.M., Gonzalez-Partida, E., Villanueva-Estrada, R.E. 2011. A model of boiling for fluid inclusion studies: Application to the Bolanos Ag-Au-Pb-Zn epithermal deposit, Western Mexico. J. Geochem. Explor. 110, 118-125.

Cetinkaya, N., Karul, B., Yenigun, K., Onal, R., 1983. Report of Turkish–Germany project Biga Peninsula on the research project of metallic mines (Pb–Zn–Cu). Mineral Research and Exploration Institute of Turkey (MTA), Report No. 7745.

Dong, G., Morrison, G., Jaireth, S., 1995. Quartz textures in epithermal veins, Queensland; Classification, origin and implication, Economic Geology, 90, 1841-1856.

Ercan, T., Satir, M., Dora, G., Sarifakioglu, E., Adis, C., Walter, H., Yildirim, T., 1995, Characteristic if Tertialy volcanismin the Biga Peninsula and Gokceda, Bozcada and Tavsan islands (NW Anatolia). Bull. Miner. Res. Explor. Inst. Turkey, 117, 55-86 (in Turkish with English abstract).

Frelinger, S.N., Ledvina, M.D., Kyle, J.R., Zhao, D. 2015. Scanning electron microscopy cathodolunnescence of quartz: Principles, techniques and applications in ore geology. Ore Geology Reviews, 65, 840-852.

Gammons, C.H. & Williams-Jones, A.E. 1997. Chemical mobility of gold in the porphyry-epithermal environment. Econ. Geol. 92, 45-59.

Gartman, A., Hannington, M., Jamieson, J.W., Peterkin, B., Garbe-Schonberg, D., Findlay, A.J., Fuchs, S., Kwasnitschka, T., 2018. Boiling induced formation of colloidal gold in black smoker hydrothermal fluids. Geology 46, 39-42.

Gotze, J., 2009. Chemistry, textures and physical properties of quartz–geological interpretation and technical application. Mineralogical magazine, 73(4), 645-671.

Guillong, M., Meir, D.L., Allan, M.M., Heinrich, V.A., Yardley, B.W.D., 2008. Sills: a Matlab based program for the reduction of Laser Ablation ICP-MS data of homogeneous materials and inclusions, Miner. Assoc. Can. Short Course 40, 328-333.

Gulyuz, N., Shipton, Z.K., Kuscu, I., Lord, R.A., Kaymaker, H., Guluz, E., Gladwell, D.R., 2018. Repeated reactivation of clogged permeable pathways in epithermal gold deposits: Kestanelik epithermal vein system, NW Turkey, Journal of the Geological Society, 175(3), 509-524.

Hannington, M., Haroardottir, V., Garbe-Schonberg, D., Brown, K.L., 2016. Gold enrichment in active geothermal systems by accumulating colloidal suspensions, Nature Geoscience, 9, 299-302.

Heinrich, C.A., 2005. The physical and chemical evolution of low-salinity magmatic fluids at the porphyry to epithermal transition: a thermodynamic study. *Mineralium Deposita, 39*, 864-889.

Heinrich, C.A., Dreisner, T., Stefansson, A., Seward, T.M. 2004. Magmatic vapor contraction and the transport of gold from the porphyry environment to epithermal ore deposits. Geology, 32, 761-764.

Henley, R.W., Berger, B.R., 2011. Magmatic-vapor expansion and the formation of high sulphidation gold deposits: Chemical controls on alteration and mineralization. Ore Geology Reviews, 39, 63-74.

Herrington, R.J. and Wilkinson, J.J., 1993. Colloidal gold and silica in mesothermal vein systems. Geology, 21, 539-542.

Hurtig, N.C. and Williams-Jones, A.E. 2015. Porphyry-epithermal Au-Ag-Mo ore formation by vapor-like fluids: New insights from geochemical modelling. Geology, 43, 587-590.

Imer, E.U., Gulec, N., Kuscu, I., Fallick, A.E., 2013, Genetic investigation and composition of Kartaldag and Madendag epithermal gold deposits in Cannakale, NW Turkey. Ore Geology Reviews, 53, 204-222.

Jankovic, S., 1986. Tethyan Eurasian Metallogenic Belt: relations of mineral associations and their tectonic setting,. Geotecton. Metallog. 10, 99-124.

Jingwen, M., Pirajno. F., Lehmann, B., Maocheng, L., Berzina, A., 2103. Distribution of porphyry deposits in the Eurasian continent and their corresponding tectonic settings. Journal of Asian Earth Sciences. 79(B), 576-584.

Kumral, M., Abdelnasser, A., Budakoglu, M., 2016, Geochemistry of hydrothermal alteration associated with Cenozoic intrusion-hosted Cu-Pb-Zn mineralization at Tavsanli area, Kutahya, NW Turkey, Minerals, 6, 1-23.

Lambrecht, G. and Diamond, L.W. 2014. Morphological ripening of fluid inclusions and coupled zone-refining in quartz crystals revealed by cathodoluminescence imaging: Implications for CL-petrography, fluid inclusion analysis and trace element geochemistry. *Geochimica et Cosmochimica Acta,* 141, 381-406.

Landtwing, M.R., Furrer, C., Redmond, P.B., Pettke, T., Guillong, M., Heinrich, C.A. 2010. The Bingham Canyon porphyry Cu-Mo-Au deposit. III. Zoned copper-gold ore deposition by magmatic vapour expansion. Economic Geology, 105, 91-118.

Lehmann, K., Berger, A., Gotte, T., Ramseyer, K., Wiedenbeck, M., 2009. Growth related zonations in authigenic and hydrothermal quartz characterized by SIMS-, EPMA-, SEM-CL and SEM-CC imaging. Mineralogical Magazine, 73, 633-643.

Lloyd, G.E., 1987. Atomic number and crystallographic contrast images with the SEM: a review of backscattered electron techniques, Mineralogical Magazine, 51, 3-19.

Moncado, D., Mutchler, S., Nieto, A., Rimstidt, J.D., Bodnar, R.J., 2012. Mineral textures and fluid inclusion petrography of the epithermal Ag–Au deposits at Guanajuato, Mexico: Application to exploration. Journal of Geochemical Exploration, 114, 20–35.

Nadeau, O., Stix, J., Williams-Jones, A.E. 2016. Links between arc volcanoes and porphyry-epithermal ore deposits. Geology. 44, 11-14.

Okay, A.I., Siyako, M., Burkan, K.A., 1990. Geology and tectonics of the Biga Peninsula. Turkey. Assoc. Pet. Geol. Bull. 2, 83–121 (in Turkish with English abstract).

Orgün, Y., Gültekin, A.H., Önal, A., 2005. Geology, mineralogy and fluid inclusion data from the Arapuçan Pb–Zn–Cu–Ag deposit, Çanakkale, Turkey. J. Asian Earth Sci. 25, 629–642.

Oyman, T., Minarecci, F., Piskin., 2003. Efemcukuru B-rich epithermal gold deposit (Izmir, Turkey), Ore Geology Reviews, 23, 35-53.

Ozen, Y. and Arik, F. 2013. Fluid inclusion and sulfur isotope thermometry of the Inkaya (Simav-Kutahya) Cu-Pb-Zn-(Ag) mineralization, NW Turkey. Central European Journal of Geosciences, 5(3) 435-449.

OzenY. and Arik, F. 2015. S, O and Pb isotopic evidence on the origin of the Inkaya (Simav-Kutahya) Cu-Pb-Zn-(Ag) prospect, NW Turkey. Ore Geology Reviews, 20, 262-280.

Pokrovski, G.S., Akinfiev, N.N., Borisova, A.Y., Zotoz, A.V., Kouzmanov, K. 2014. Gold speciation and transport in geological fluids: insights from experiments and physical-chemical modelling. Geol. Soc. London, Spec. Publ. 402, 9-70.

Pudack, C., Halter, W.E., Heinrich, C.A., Pettke, T. 2009. Evolution of magmatic vapor to gold-rich epithermal liquid: The porphyry to epithermal transition at Nevados de Famatina, Northwest Argentina. Economic Geology, 104, 449-477.

Reed, M.H., Palandri, J., 2006. Sulphide mineral precipitation from hydrothermal fluids. Rev. Mineral. Geochem. 61, 609-631.

Richards, J.P., 2013. Giant ore deposits formed by optimal alignments and combinations of geological processes. Nat. Geosci. 6, 911-916.

Richards, J.P. 2015. Tectonic, magmatic and metallogenic evolution of the Tethyan orogeny: From subduction to collision. Ore Geology Reviews, 70, 323-345.

Rottier, B., Kouzmanov, K., Casanova, V., Walle, M., Fontbote, L. 2018. Cyclic dilution of magmatic low-salinity fluid: A major process generating the giant epithermal polymetallic deposit of Cerro de Pasco, Peru, Economic Geology, 113, 825-856.

Rusk, B., Reed, M. 2002. Scanning electron microscope-cathodoluminescence analysis quartz reveals complex growth histories in veins from the Butte porphyry copper deposit, Montana. Geology, 30, 727-730.

Sander, M.V., Black, J.E., 1988. Crystallization and recrystallization of growth-zoned vein quartz crystals from epithermal systems: Implications for fluid inclusion studies. Economic Geology, 83, 1052-1060.

Saunders, J.A., 1990. Colloidal transport of gold and silica in epithermal precious-metal systems: Evidence from the Sleeper deposit, Nevada. Geology, 18, 757-760.

Saunders, J.A., Schoenly, P.A. 1995. Boiling, colloidal nucleation and aggregation, and the genesis of bonanza Au-Ag ores of the Sleeper deposit, Nevada. Mineralium Deposita, 30, 199-210.

Saunders, J.A. 2012. Textural evidence of episodic introduction of metallic nanoparticles into bonanza epithermal ores. Minerals, 2, 228-243.

Sanchez, M. G., McClay, K., King, A. 2013. Tectonic and structural setting of porphyry Cu-Au and epithermal Au mineralization of the Biga Peninsula, NE Aegean, 12th Biennial SGA Meeting , Mineral Deposit Research for a Hi-Tech World, Vols. 1-4 pp: 1451-1454.

Sanchez-Alfaro, P., Reich, M., Dreisner, T., Cembrano, J., Arancibia, G., Perez-Flores, P., Heinrich, C.A., Rowland, J., Tardani, D., Lange, D., Campos, E. 2016. The optimal windows for seismically-enhanced gold precipitation in the epithermal environment. Ore Geology Reviews, 79, 463-473.

Schloglova, K., Walle, W., Heinrich, C.A. 2017. LA-ICP-MS analysis of fluid inclusion: contamination effects challenging micro-analysis of elements close to their detection limit. Journal of Analytical Atomic Spectrometry, 32, 1052-1063.

Seward, T.M. and Barnes, H.L. 1997. Metal transport in hydrothermal ore fluids. *In* Geochemistry of Hydrothermal Ore Deposits, Chapter 9, 435-486. 3rd edn. H.L.Barnes (editor), Wiley and Sons.

Sibson, R.H., 1987. Earthquake rupturing as a mineralizing agent. Geology, 15, 701-704.

Sibson, R.H., Robert, F., Poulsen, K.H. 1988. High-angle reverse faults, fluid-pressure cycling, and mesothermal gold-quartz deposit. Geology, 16, 551-555.

Simmons, S.F. and Brown, K.L,. 2006. Gold in magmatic hydrothermal solutions and the rapid formation of a giant ore deposit. Science, 314, 288-291.

Smith, M.T., Lepore, W.A., Incekaraoglu, T., Shabestari, P., Boran, H., Raabe, K., 2014. Kucukdag: A new high sulphidation epithermal Au-Ag-Cu deposit at the TV Tower property in western Turkey. Economic Geology, 109, 1501-1511.

Taran, Y.A., Bernard, A., Gavilanes, J.C., Africano, F. 2000. Native gold in mineral precipitates from high temperature volcanic gases of Colima volcano, Mexico. Appl. Geochem. 15, 337-346.

Tosdal, R.M., Dilles, J.H., Cooke, D.R. 2009. From source to sink in auriferous magmatic-hydrothermal porphyry and epithermal deposits. Elements, 5, 289-295.

Ulrich, T., Gunther, D., Heinrich, C.A. 1999. Gold concentration of magmatic brines and the metal budget of porphyry copper deposits. Nature, 399, 676-679.

Unal, E.I., Gulec, N., Kuscu, I. and Fallick, A.E., 2013. Genetic investigation and comparison of Kartaldag and Madendag epithermal gold deposits in Çanakkale, NW Turkey. Ore Geology Reviews, 53. 204–222.

Urai, J.L., Williams, P.F., van Roermund, H.L.M. 1991. Kinematics of crystal growth in syntectonic fibrous veins, Journal of Structural Geology, 13(7), 823-836.

Van den Kerkhof, A.M., and Hein, U.F., 2001. Fluid inclusion petrography, Lithos, 55, 27-47.

Weatherley, D.K. and Henley, R.W., 2013. Flash vaporization during earthquakes evidenced by gold deposits. Nature Geoscience, 6, 294-298.

White, J.F., and Corwin, J.F., 1961. Synthesis and origin of Chalcedony. American Mineralogist, 46, 112-119.

Wilkinson, J.J. and Johnston, J.D., 1996. Pressure fluctuations, phase separation, and gold precipitation during seismic fracture propagation. Geology, 24, 395-398.

Williams-Jones, A.E., Bowell, R.J., Migdisov, A.A. 2009. Gold in solution. Elements, 5, 281-287.

Yigit, O., 2006. Gold in Turkey – a missing link in Tethyan Metallogeny, Ore Geology Reviews, 28, 147-179.

Yigit, O., 2009. Mineral deposits of Turkey in relation to Tethyan Metallogeny: Implications for future mineral exploration, Economic Geology, 104, 19-51.

Yigit, O., 2012. A prospective sector in the Tethyan Metallogenic Belt: Geology and geochronology of mineral deposits in the Biga Peninsula, NW Turkey, Ore Geology Reviews, 46, 118-148.

Yilmaz, Y., 1990. Allochtonous terrains in the Tethyan Middle East, Anatolia and the surrounding regions. Phil Trans. Roy. Soc. London, A331, 611-624.

Yilmaz, H., 2002. Ovacik gold deposit: An example of quartz-adularia type gold mineralization in Turkey. Economic Geology, 97, 1829-1839.

Yilmaz, H., Oyman, T., Sonmez, F.N., Arehart, G.B., Billor, Z., 2010. Intermediate sulphidation epithermal gold-base metal deposits in Tertiary subaerial volcanic rocks, Sahinli/Tespih Dere (Lapseki/western Turkey). Ore Geology Reviews, 37, 236-258.

Yilmaz, H., Sonmez, F.N., Akay, E., Sener, A.K., Tufan, S.T., 2013. Low-sulfidation epithermal Au-Ag mineralizationin the Sindirgi District, Balikeshir Province, Turkey. Turkish Journal of Earth Sciences, 22, 485-522.

Yücelay, M.A., 1971. Geological etude of the Karaköy-Arapuçandere Pb–Zn–Cu mineralization, Çanakkale-Yenice. Mineral Research and Exploration Institute of Turkey, Report No. 4688.

Yudovskaya, M.A., Distler, V.V., Chaplygin, I.V., Mokhov, A.V., Trubkin, N.V., Gorbacheva, S.A., 2006. Gaseous transport and deposition of gold in magmatic fluid: evidence from the active Kudryavy volcano, Kurile Islands. Mineral. Deposita, 40, 828-848.

Zajacz, Z., Candela, P.A., Piccoli, P.M., 2017. The partitioning of Cu, Au and Mo between liquid and vapor at magmatic temperatures and its implication for the genesis of magmatic-hydrothermal ore deposits. Geochimica et Cosmochimica Acta, 207, 81-101.

Zezin, Y.D., Migdisov, A.A., Williams-Jones, A.E., 2011. The solubility of gold in H_2O-H_2S vapour at elevated temperature and pressure. Geochim. Cosmochim. Acta 75, 5140-5153.

Figure Captions

Figure 1. Section of mineralized vein showing the context of the quartz crystals studied studied. (a) Massive sulphides in meta-diabase wallrock with large euhedral quartz crystals. The sample is in the Canakkale 18 Mart University's Earth Science Museum. (b) Example of the euhedral quartz crystals from which the samples in this study were taken.

Figure 2. Quartz textures related with trapping of fluid inclusions. (a, b) ppl and xpl images of zoned quartz perpendicular to the c-axis. The dark striations around the crystal faces are

areas of fluid inclusions. Early euhedral quartz followed by more anhedral quartz. (c) xpl image of part of a euhedral quartz crystal with areas of intense black striations of fluid inclusions. (d, e) ppl and xpl images of sector zoned quartz crystals, perpendicular to the c-axis. Radiating fibrous growth of quartz from rhomb faces, is delineated by dark bands of dense accumulations of primary fluid inclusions and light areas which are dominantly quartz.

Figure 3. (a) 250 μm thick doubly polished fluid inclusion wafer of the whole quartz crystal. (a) Normal illumination from above shows different areas of fluid inclusions as light areas. (b) CL mosaic image of 2.5 mm squares showing growth textures and the location fluid inclusions measured, with average salinities. Values in the yellow boxes are areas where fluid inclusions were analysed by LA-ICP-MS.

Figure 4. SEM-CL images of growth textures relative to fluid inclusions. (a) Top left of figure 3b where the black area of fluid inclusions between the two distinctive crystal faces relates to patches of inclusions as in figure 5b. (b) top right where long elongate trails of fluid inclusions are seen to originate at distinct crystal growth faces. (c) Black lines indicate the termination of quartz growth. The trail of V-rich inclusions, figure 5f, cuts the crystal starting at opposite sides, but does not penetrate the next growth of quartz. The next quartz has grown with a comb-like texture compared to the euhedral growth of the preceding quartz. (d) Intense chaotic trapping of fluid inclusions on top of euhedral quartz which is largely devoid of inclusions.

Figure 5. Types and occurrences of fluid inclusions. (a) Trails of elongate inclusions trapped between fibrous quartz. Location is the inclusions in figure 4b.(b) Random areas of fluid inclusions with variable L/V ratios. Corresponds to the inclusions between growth zones in figure 4a. (c) L-V plus solid. (d) Vapour inclusion. (e) Large V-rich inclusion with a small amount of liquid. (f) Part of V-rich pseudosecondary trail in figure 4c.

Figure 6. Distribution of salinity and homogenization temperature from inclusions measured in areas shown in figure 3b. (a) Gaussian distribution of inclusions that homogenize to liquid or vapour. (b) Bi-modal distribution of salinities with a tail extending to higher values.

Figure 7. Fluid inclusion salinity vs homogenization temperature pairs have 3 groups. There is no relation between Th and salinity. Salinities of greater than 6 wt.% NaCl equiv. are from secondary inclusions.

Figure 8. SEM images of particulate gold. (a) BSE image of 2 large opened fluid inclusions, from the area in figure 4b, bright spots corresponding to Au, with Ba, Pb and Fe also present. (b) Enlarged area with a number of gold particles, brightest rounded grains. (c) BSE element maps of the largest c.1.5 μm particle, for Au, Ag and Cu.

Figure 9. (a) BSE image of an open fluid inclusion in quartz. Many sub-micron Au-grains (indicated by yellow arrows) sit on calcite precipitated the inner surface. (b) SE image of (a) showing the sub-crystalline nature of the calcite precipitate on the walls of the fluid inclusion.

Figure 10. Composite element map of a large open fluid inclusion and individual element distributions. Ca and S coat a large proportion of the inclusion. Individual crystals of other elements are present.

Figure 11. LA-ICP-MS profiles of fluid inclusions. (a) Sequence of 3 inclusions show the signal for Au is only present with Na and K from the fluid inclusions. Continued ablation shows no gold in the quartz matrix. (b) The asymmetrical signal from Au is matched by Ag and is within the fluid inclusion signal

Figure 12. Distribution of Au and Ag concentrations measured in fluid inclusions and quartz by LA-ICPMS. The data covers several orders of magnitude and likely reflects missing heterogeneous trapping of Au-Ag particles and particles that were not analysed in the ICP-MS. Analyses from open inclusions are omitted. The detection limits for Au and Ag related to analyses of fluid inclusions.

Figure-1

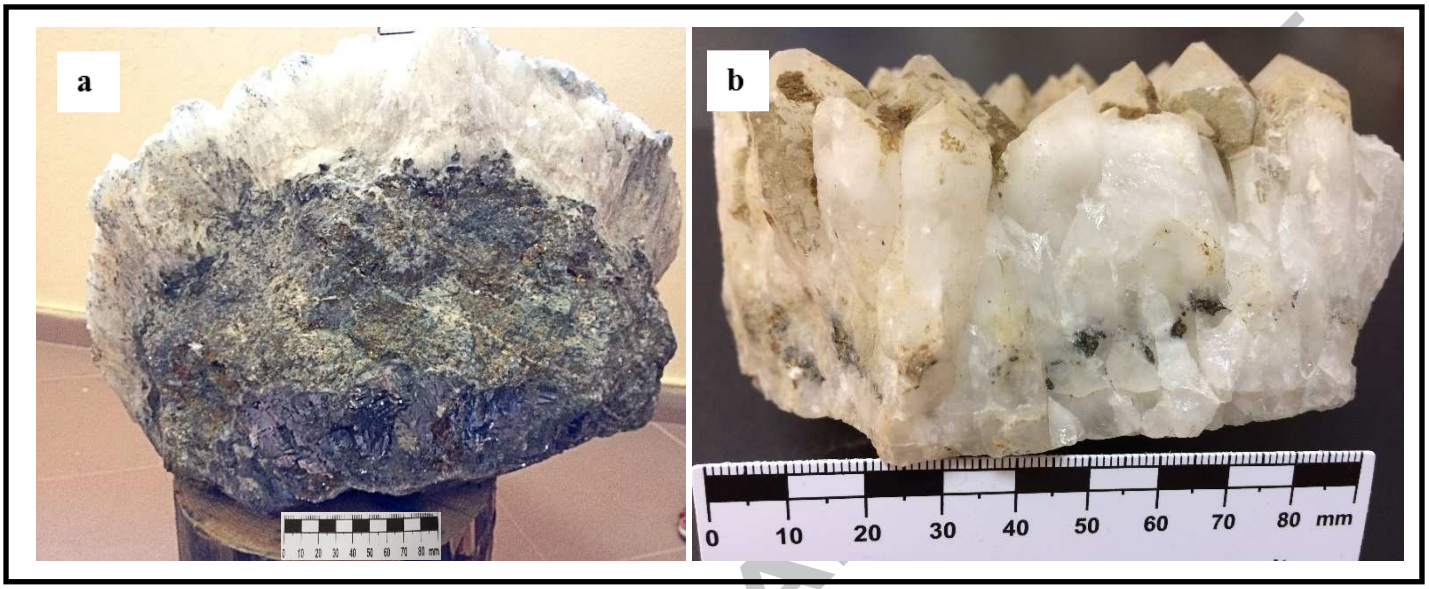

Figure-2

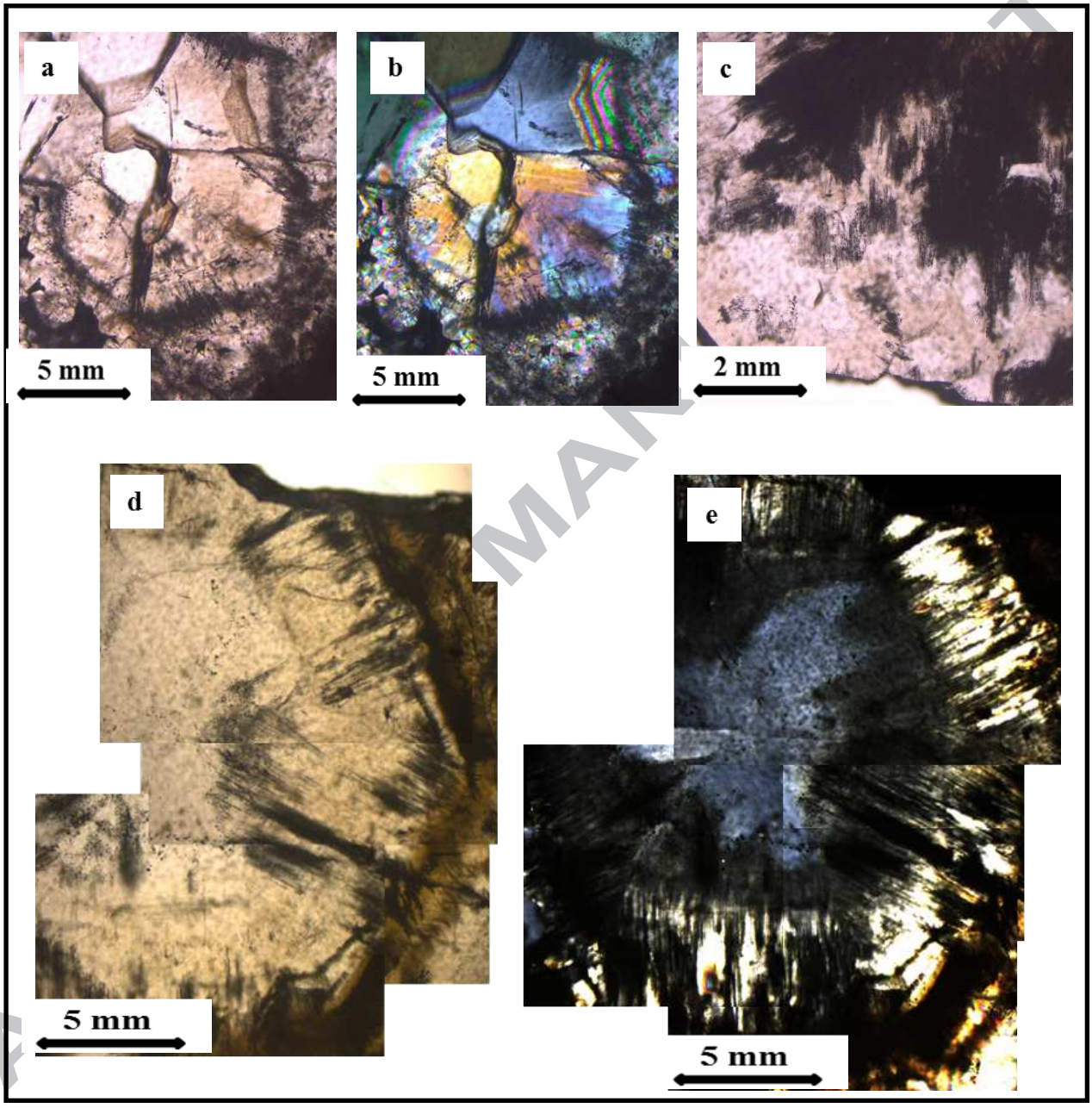

Figure-3

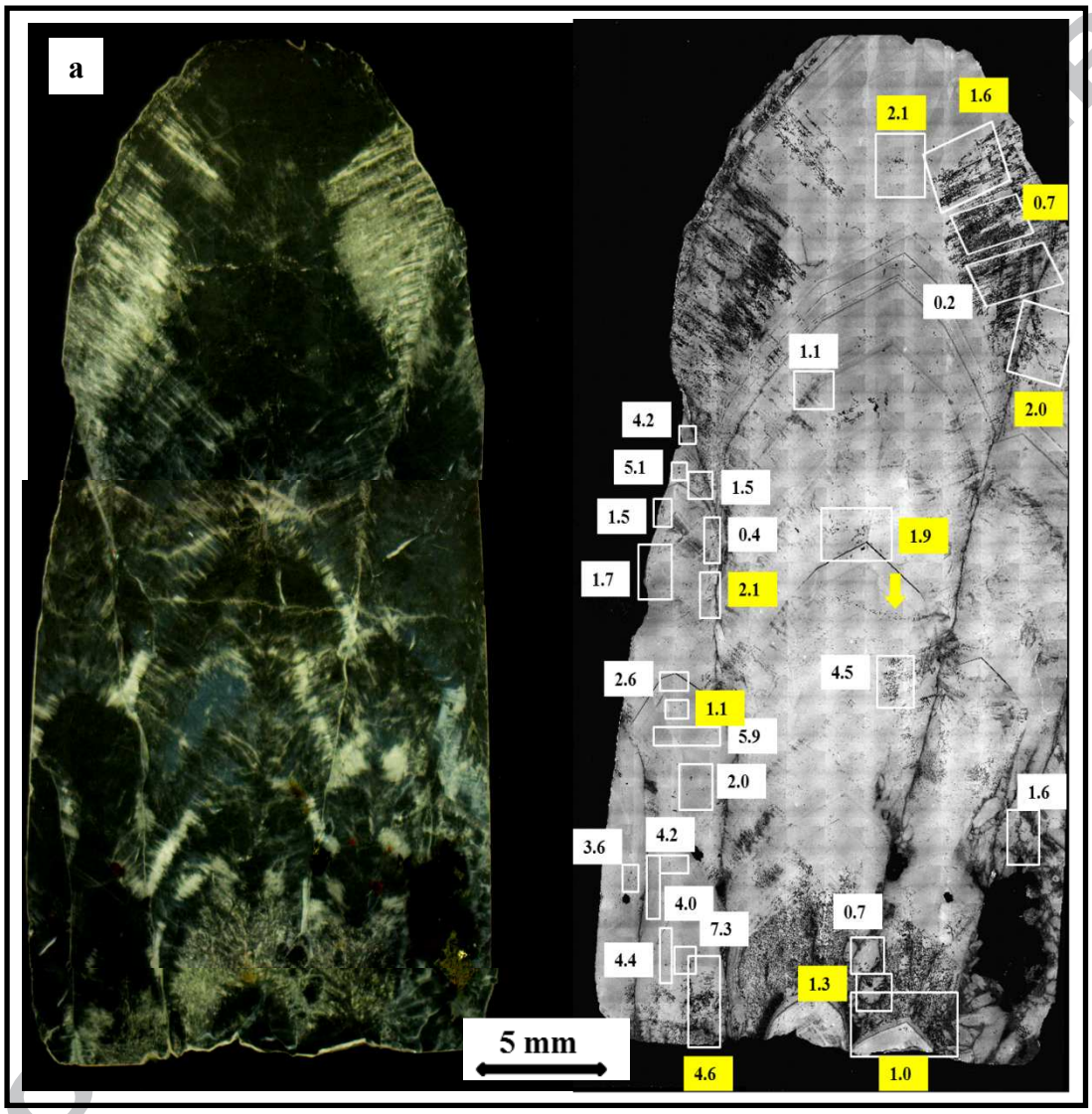

Figure-4

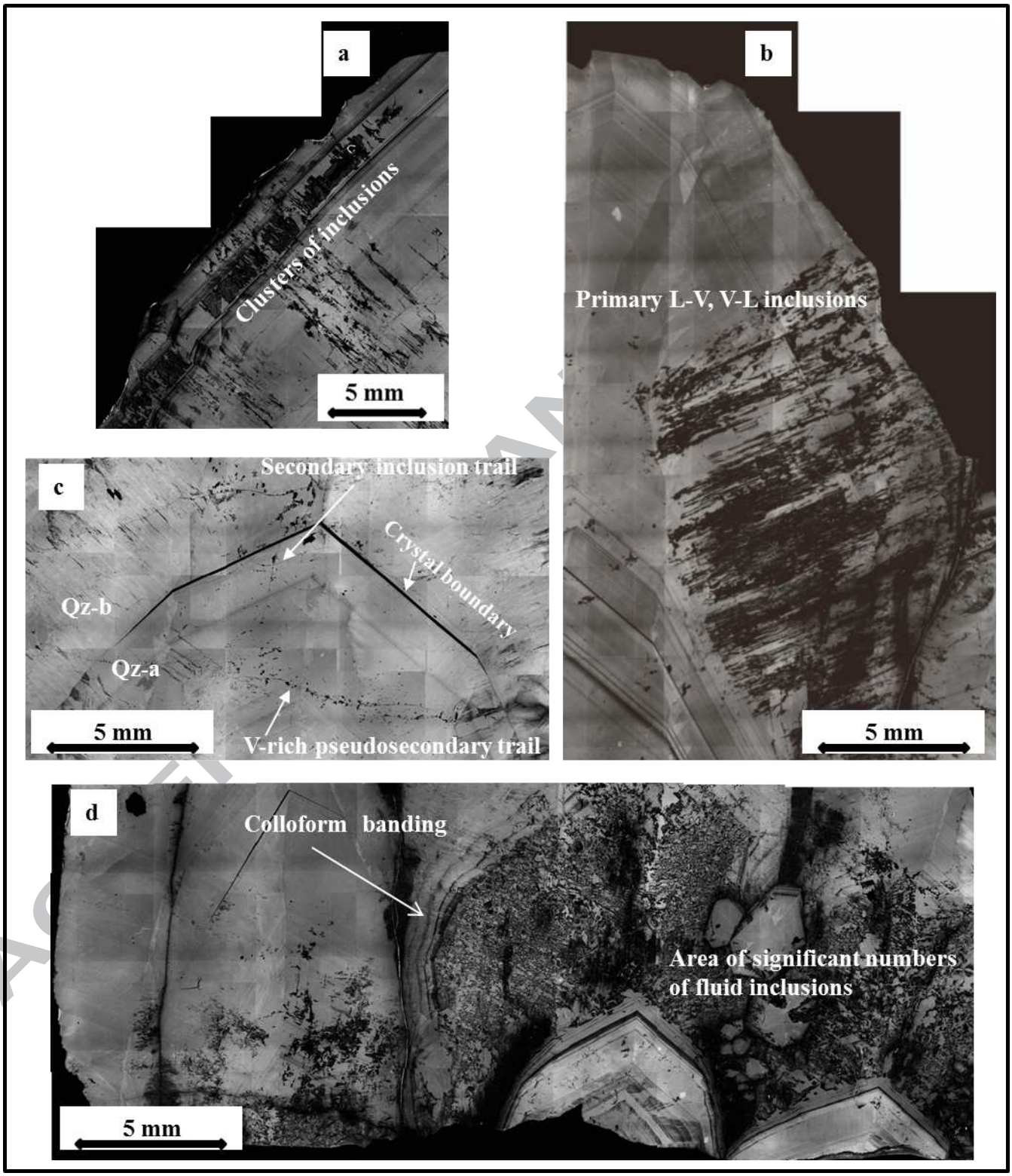

Figure-5

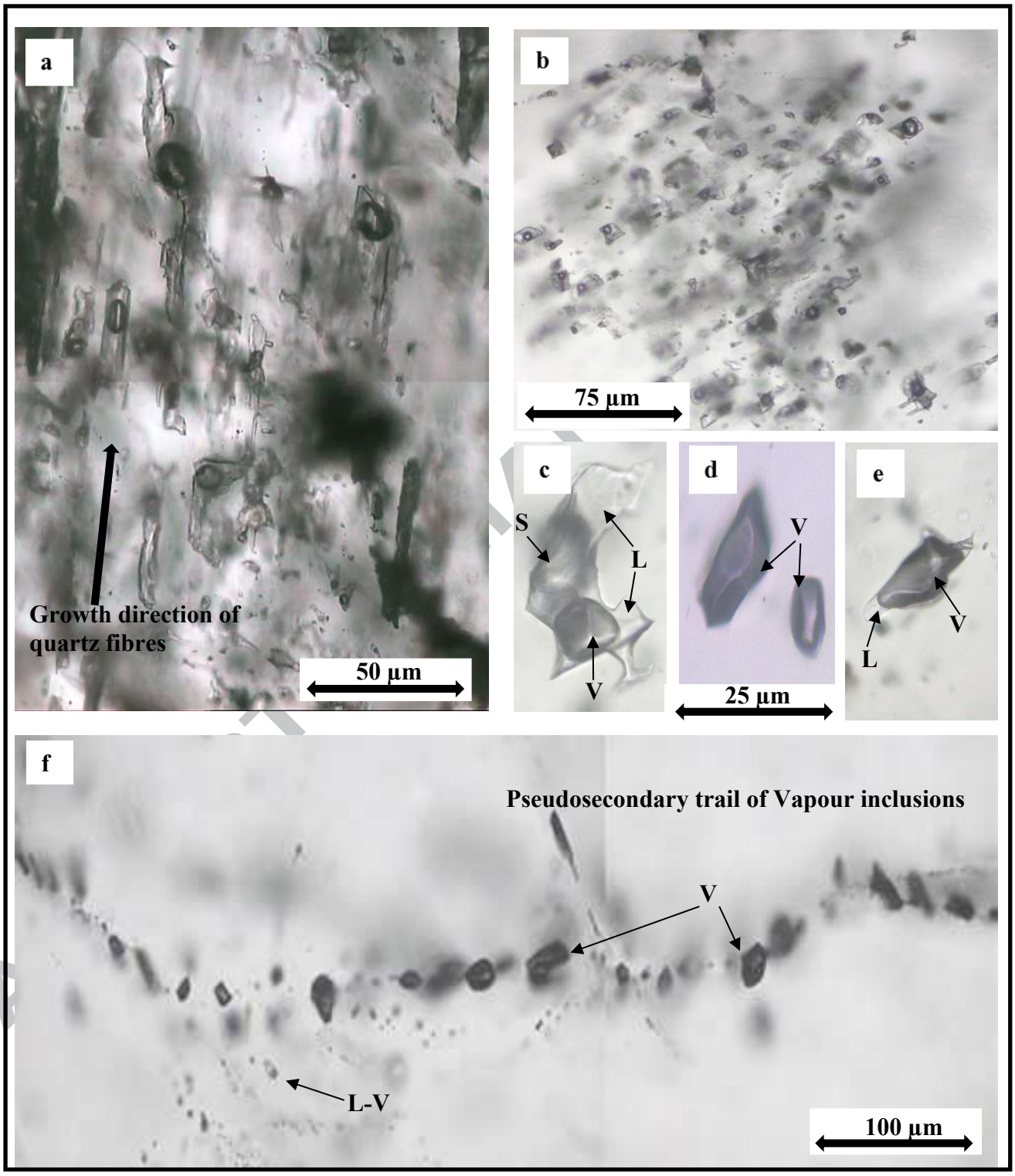

Figure-6

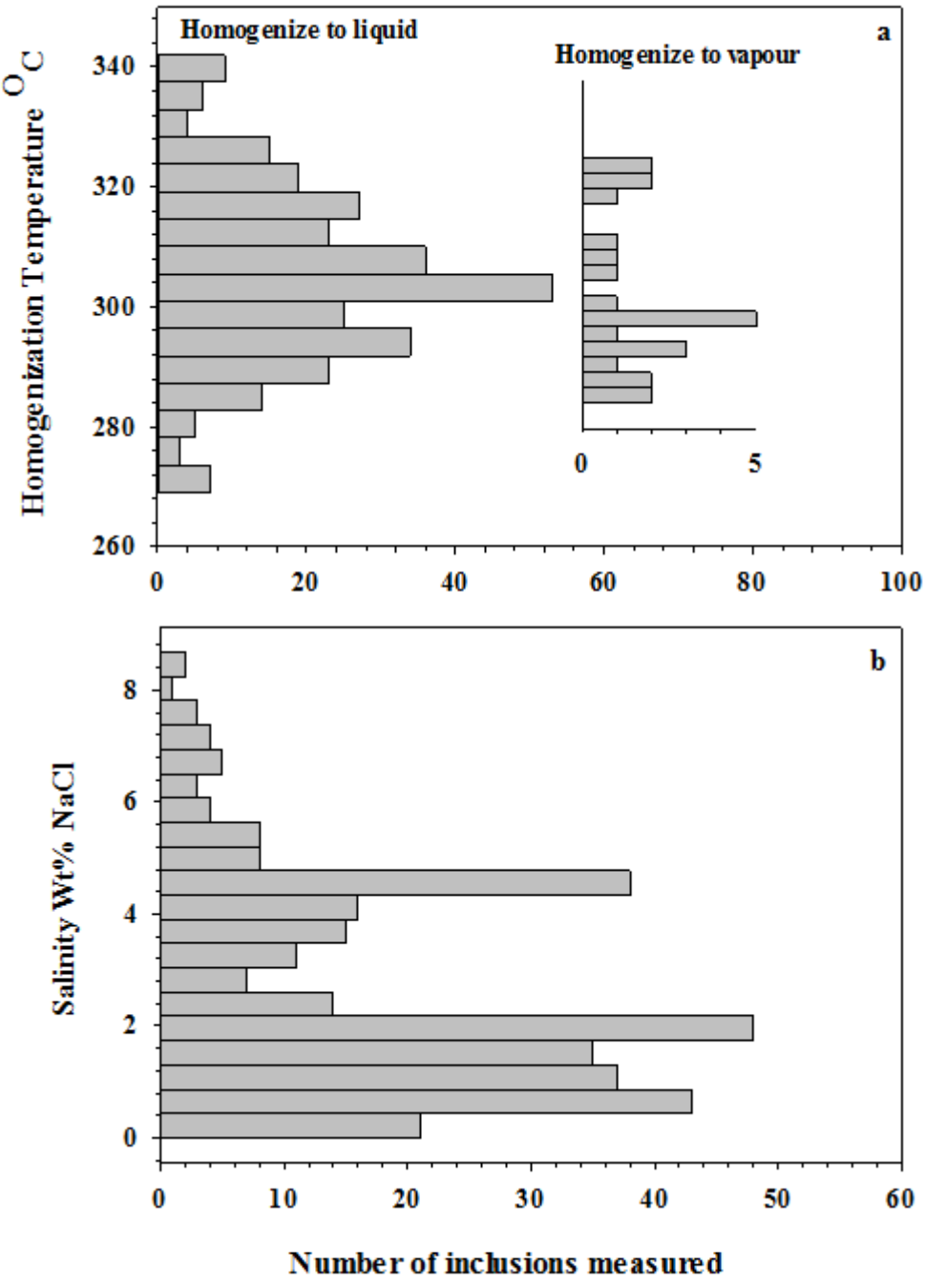

Figure-7

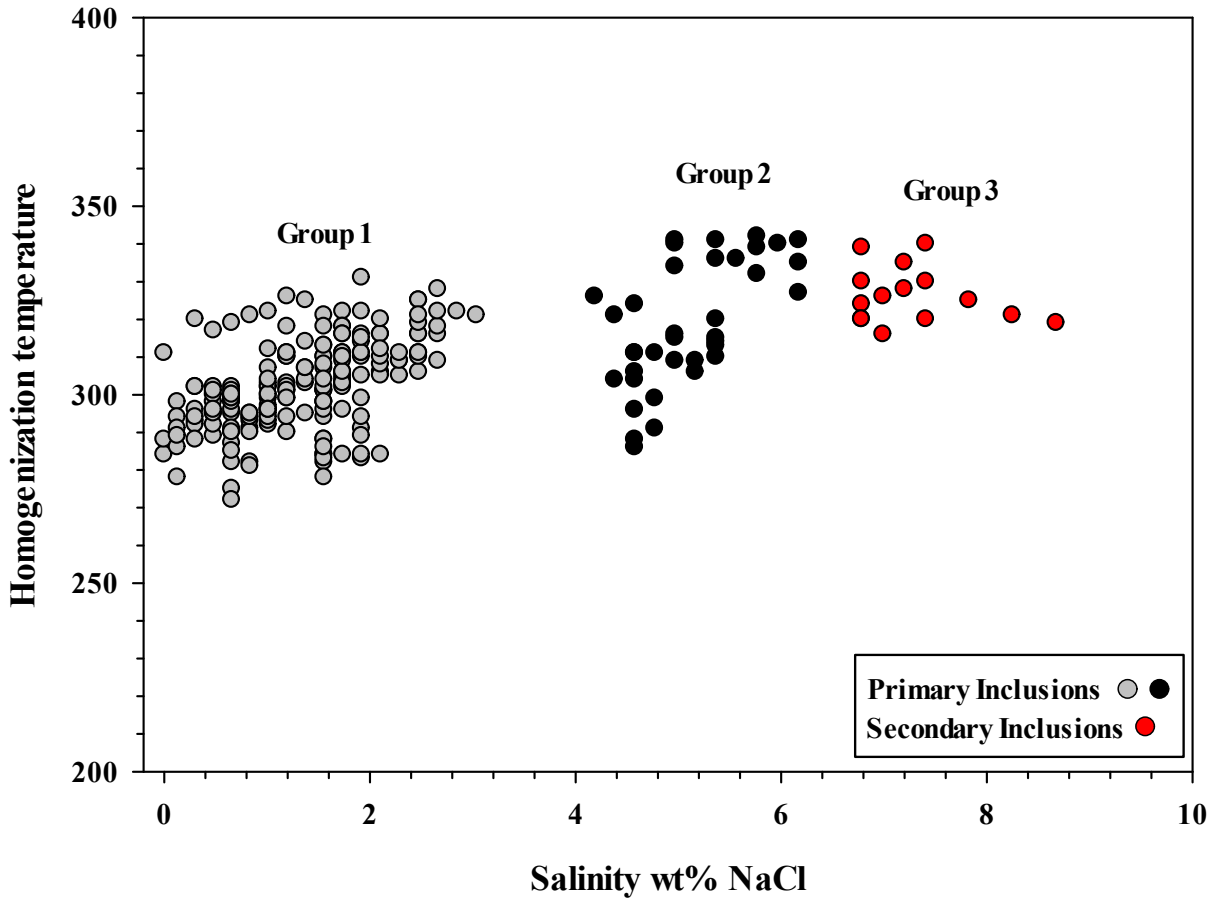

Figure-8

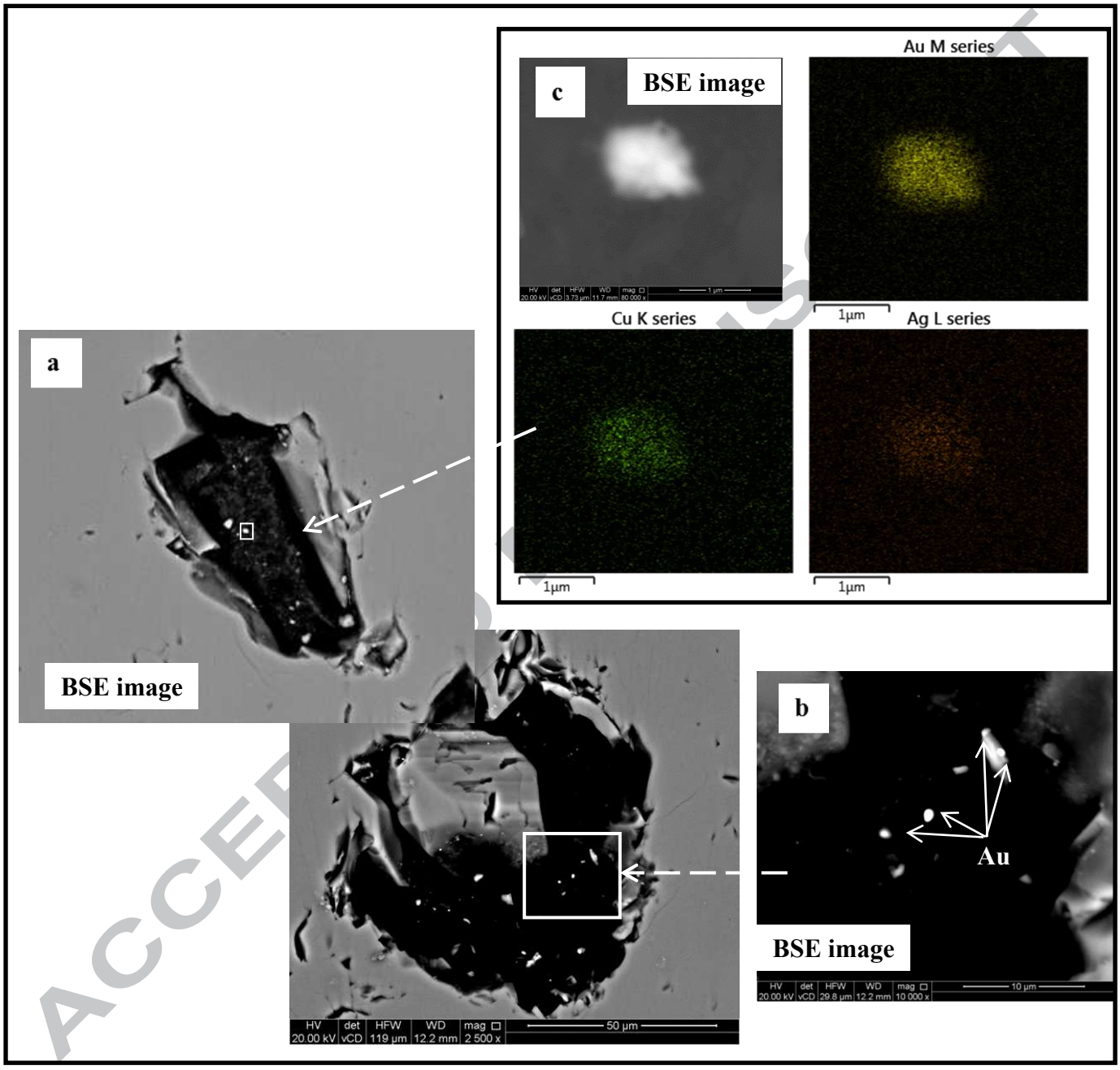

Figure-9

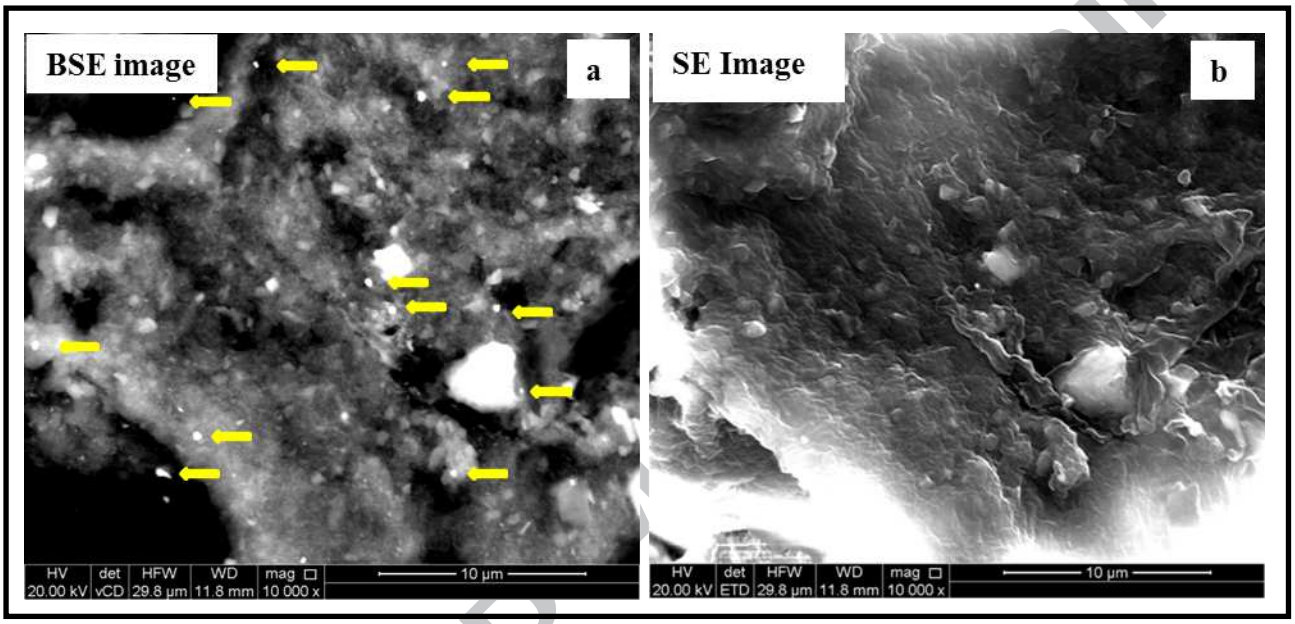

Figure-10

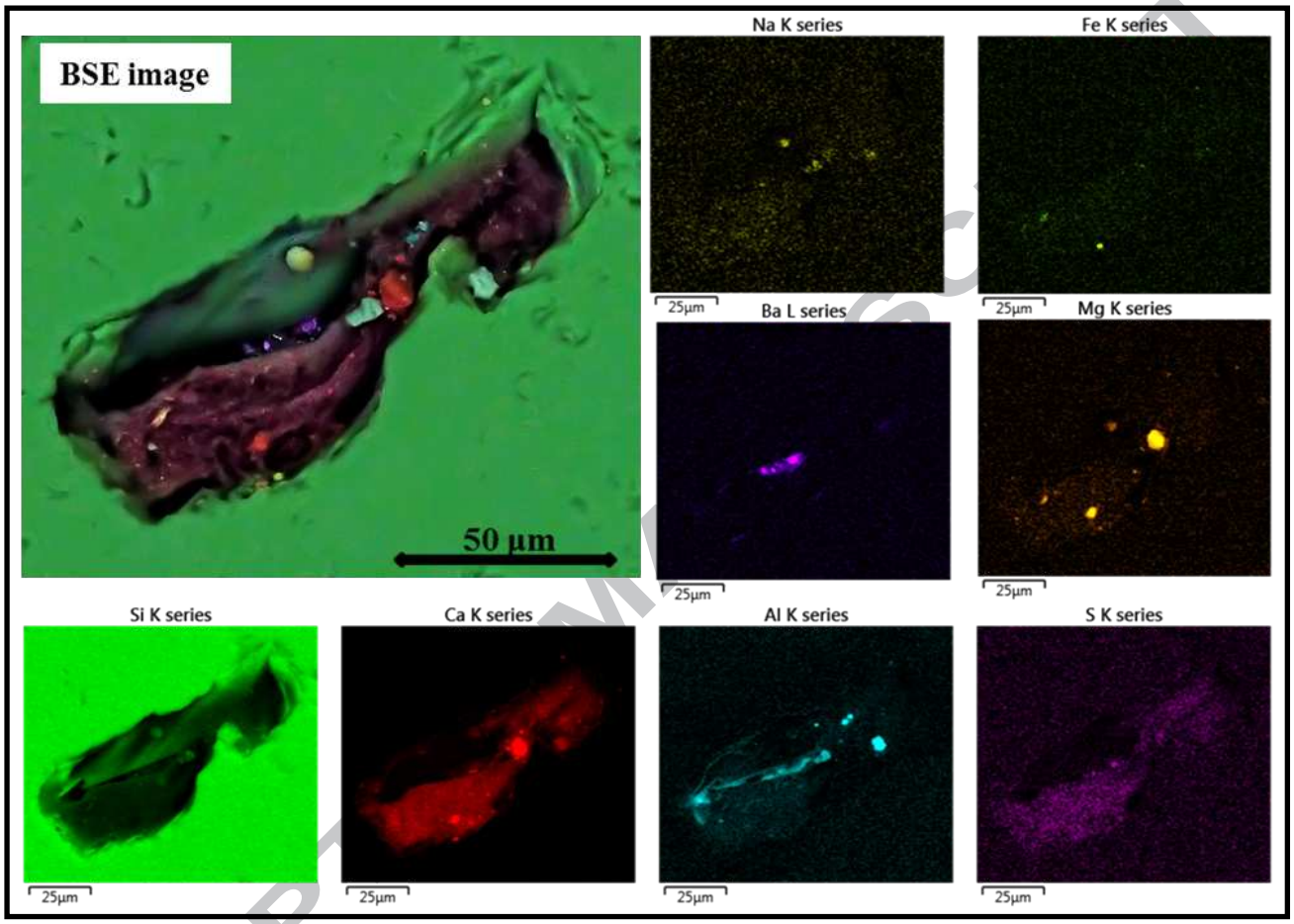

Figure-11

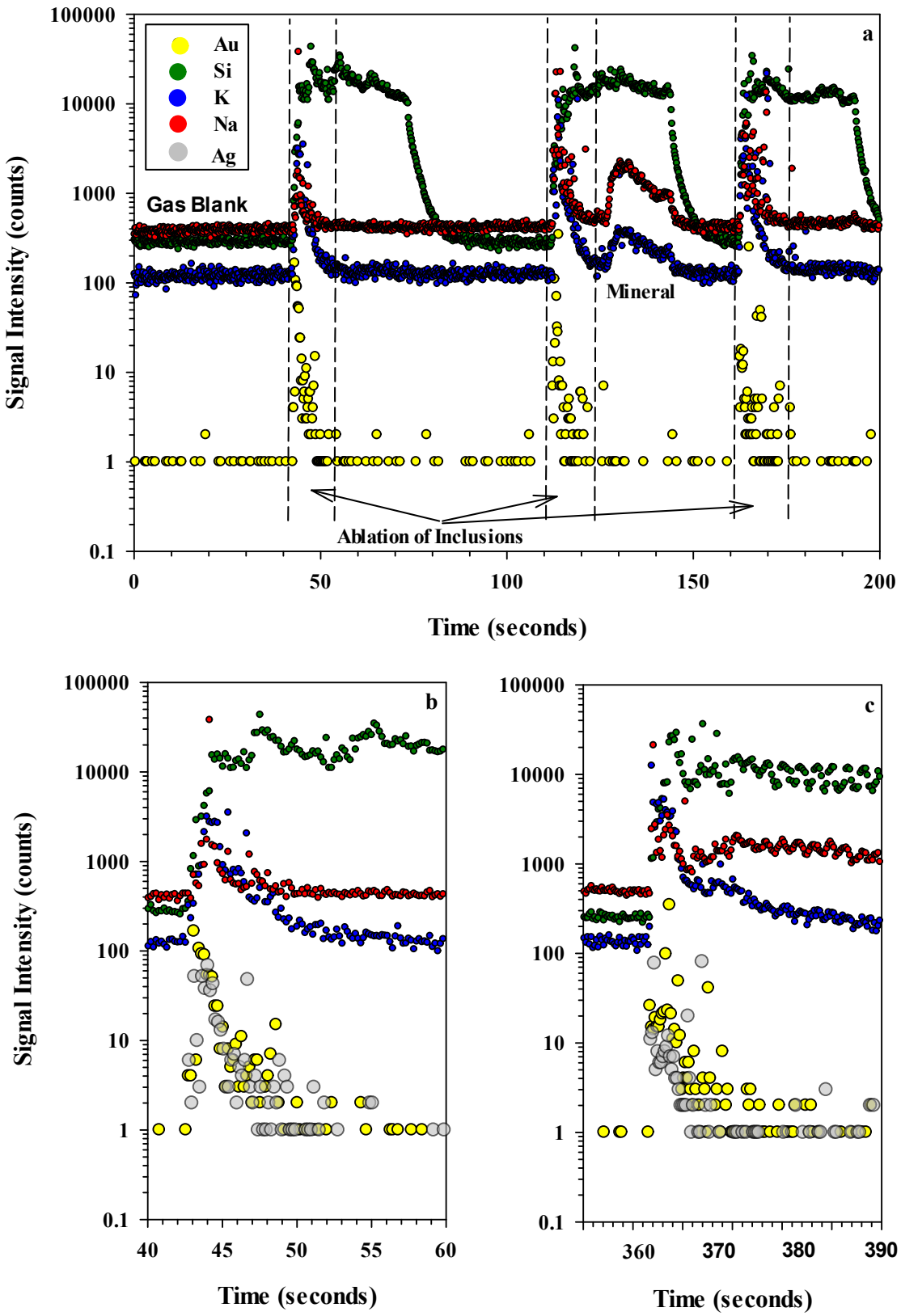

Figure-12

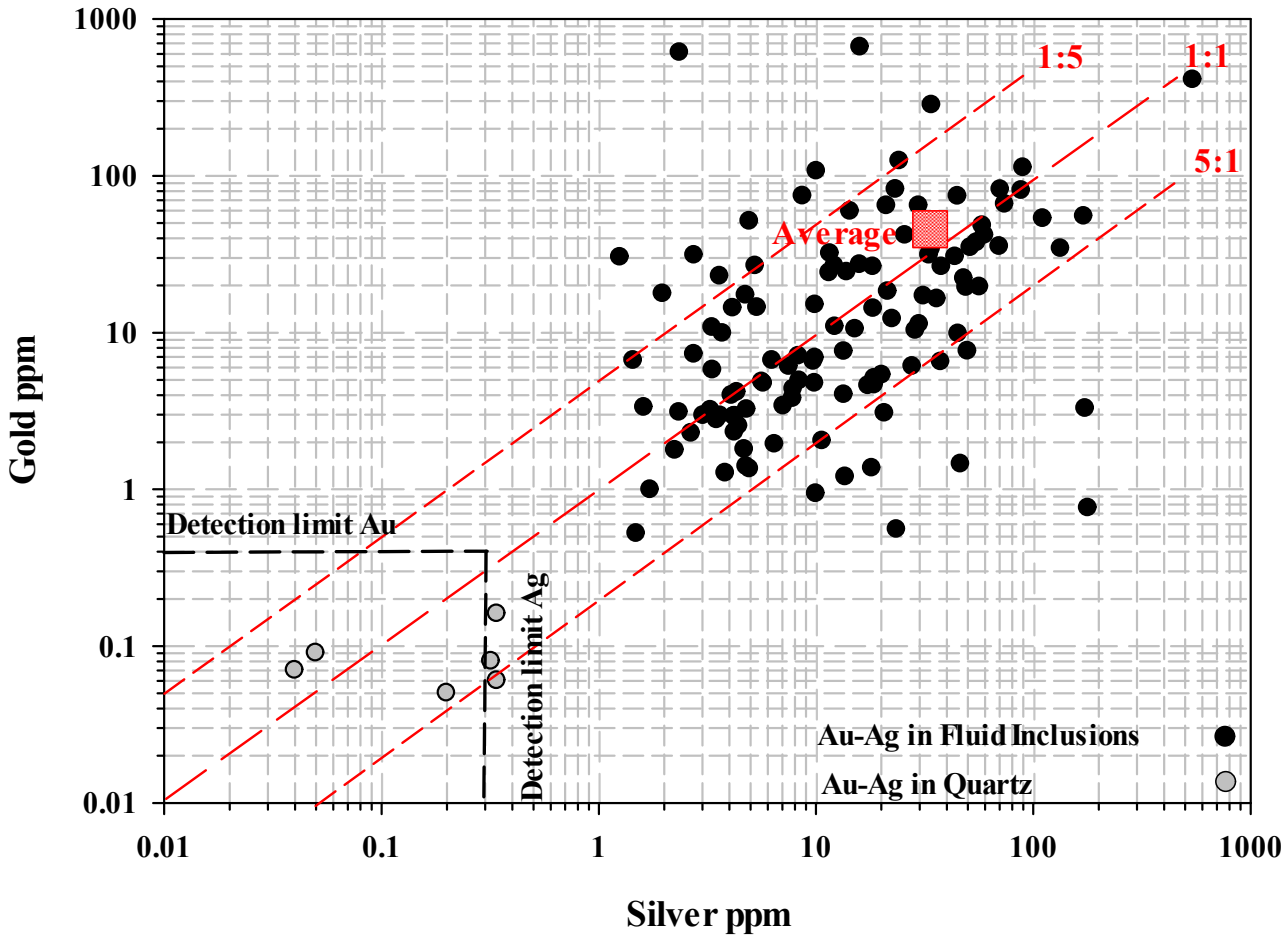

Table 1. Average composition of LA-ICPMS analyses (ppm) of fluid inclusions in the different zones.

Area Analysed	**Salinity** wt% NaCl	**Na**	**Mg**	**K**	**Ca**	**Mn**	**Fe**	**Cu**	**Zn**	**Sr**	**Ag**	**Ba**	**Au**	**Pb**
Zone a-1	1.6	3272	432	938	1127	39	110	115	140	21	(35)	58	(27)	25
Zone a-2	0.7	1312	325	475	432	34	60	nd	55	9	(5)	17	(17)	27
Zone a-4	2.0	3870	323	1543	1230	20	247	163	175	104	(10)	127	(27)	46
Zone a-5	2.1	3935	856	1415	1394	74	193	116	152	25	(27)	60	(42)	19
Zone a-6	1.9	4112	375	653	1614	125	7	149	279	23	(34)	37	(201)	37
Zone b-1	1.0	2391	218	668	345	21	81	89	72	9	(87)	19	(4)	10
Zone b-2	1.3	2573	237	742	1147	87	76	62	42	64	(63)	62	(19)	8
Zone c-1	1.1	2264	198	1131	831	77	169	100	125	69	(13)	95	(16)	39
Zone c-2	2.1	4386	183	1417	1176	25	166	94	138	19	(15)	225	(55)	18
Zone d-1	4.6	10541	1425	2216	3158	203	587	817	629	264	(44)	nd	(39)	210
Vapour trail	1.3	3247	11	1144	148	63	85	317	45	2.8	(7)	32	(2)	5

(Ag) and (Au) analyses were not included in the calculation of the dissolved cations in the fluid inclusions. (Ag) and (Au) concentrations were calculated from their wt. /wt. ratio relative to Na and the concentration of Na in the fluid inclusions.

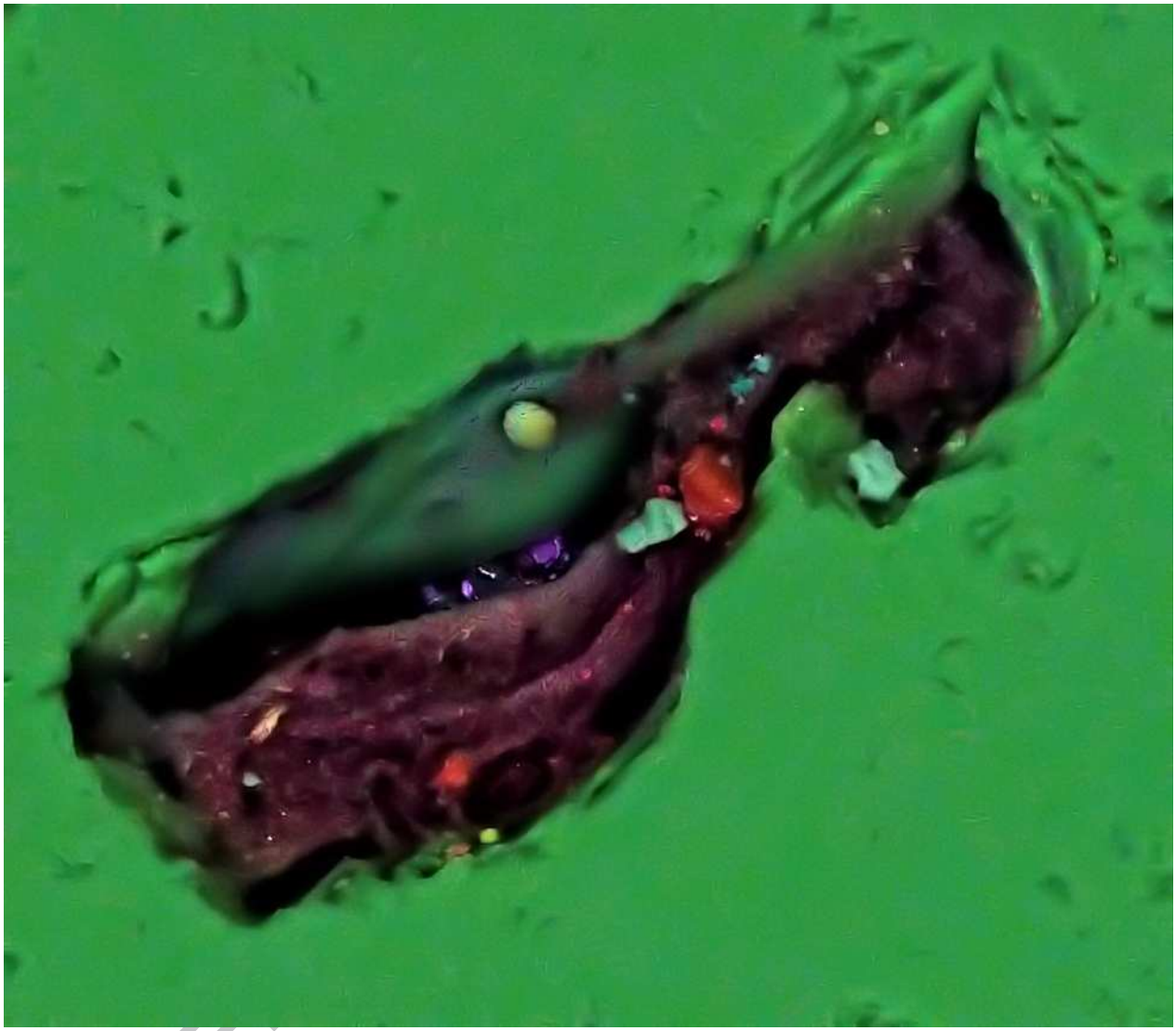

Highlights

Sub-micron colloidal gold particles visible in fluid inclusions from epithermal base-metal±Au deposit .

High concentrations of Au and Ag determined in fluid inclusions.

Transport by low density magmatic vapour.

Method of producing “bonanza grades”.